
This manuscript is a preprint and has not undergone peer-review. Please note that subsequent versions of this manuscript may have different content. If accepted, the final version of this manuscript will be available via the ‘Peer-reviewed Publication DOI’ link on the right-hand side of this webpage. Please feel free to contact any of the authors, we welcome feedback!

Shear localization as a key control on mass-transport complexes seal integrity: insights from geophysical datasets

Zhenghao Han¹, Nan Wu^{1*}, Jinfeng Ren^{2,3}, Zenggui Kuang^{2,3}

¹State Key Laboratory of Marine Geology, Tongji University, 1239 Siping Road, Shanghai, 200092, China

²National Engineering Research Center of Gas Hydrate Exploration and Development, Guangzhou Marine Geological Survey, Guangzhou, 511458, China

³Key Laboratory of Marine Mineral Resources, Ministry of Natural Resources, Guangzhou, 510075, China

*Nan Wu (nanwu@tongji.edu.cn)

Key Points:

- Shear localization occurs in MTCs base, forming a high-compaction, low-permeability zone that provides an effective seal for hydrocarbon;
- Topographic highs can disrupt shear localization, thereby reducing compaction and compromising seal integrity of MTCs above these features;
- Effective MTCs seals promote free gas or high-saturation hydrate, yet poor MTCs seals favor low-saturation hydrate coexisting with free gas.

Abstract

Mass-transport complexes (MTCs), existing in all sedimentary basins worldwide, can serve as effective seals for hydrocarbons and carbon dioxide storage due to shear-induced overcompaction. However, localized seal failure is occasionally observed in specific part of MTCs, leading to hydrocarbon and carbon dioxide leakage, and posing potential threats to seabed stability. Due to the scarcity of borehole data that penetrate MTCs, their petrophysical properties remain poorly constrained, and factors controlling their seal integrity are not well understood. This study integrates 3D seismic and well log data to investigate petrophysical characteristics of three stacked MTCs in the Qiongdongnan Basin, northern South China Sea, aiming to identify the key factors controlling their seal integrity. Seismic interpretation reveals that seal integrity of MTCs tends to fail in areas where frontal ramps or remnant blocks are present, whereas the remaining parts remain intact and effectively seal the underlying free gas and gas hydrate. Petrophysical analyses show that MTCs with frontal ramps or remnant blocks exhibit significantly lower compaction. Numerical simulations indicate that during MTC emplacement, shear localization develops in the lowermost part, forming a

31 narrow, highly deformed band. The presence of remnant blocks and frontal ramps can interrupt shear
32 localization, causing segmentation of the basal shear zone. This segmentation reduces shear strain
33 and compaction above these topographic highs, thereby compromising the seal integrity of MTCs.
34 Therefore, shear localization is the key factor controlling the seal integrity of MTCs, while
35 topographic highs can disrupt this process, significantly affecting hydrocarbon distribution and
36 feasibility of carbon dioxide storage.

37 **Plain Language Summary**

38 Submarine landslides generate mass-transport complexes (MTCs) in sedimentary basins worldwide,
39 which can seal oil, gas and carbon dioxide due to their high-compaction and low-permeability
40 characteristics. However, recent studies have observed that seal failure may occur at certain parts of
41 MTCs, which questions MTCs' reliability as effective seals. Therefore, this study aims to explore
42 the conditions under which MTCs serve as effective seals or fail. Based on 3D seismic data and
43 well log data in the Qiongdongnan Basin, South China Sea, we show that MTCs seals exhibit lower
44 compactness and fail in the presence of frontal ramps or remnant blocks. Numerical simulation
45 results further reveal that shear localization forms a highly compacted basal shear zone during
46 MTCs emplacement; however, frontal ramps and remnant blocks disrupt shear localization
47 processes, thus destroying the continuity of basal shear zone above them. As basal shear zone is
48 critical in ensuring the MTCs seal integrity, shear localization is proven to be the key controlling
49 factor on MTCs seal integrity, while topographic highs compromise MTCs seal integrity by
50 disrupting shear localization. Understanding the controlling factor on MTCs seal integrity helps
51 predict where hydrocarbons accumulate and where carbon dioxide can be stored safely in future
52 carbon neutralization initiatives.

53 **1 Introduction**

54 Mass-transport complexes (MTCs) are intensely deformed sedimentary bodies generated by the
55 downslope movement of unstable sediments under gravity (Talling et al., 2007; Bull et al., 2009;

56 Dugan, 2012). MTCs can cover areas ranging from a few square kilometers to over ten thousand
57 square kilometers, with volumes reaching up to several hundred cubic kilometers (Karstens et al.,
58 2023; Sager et al., 2022; Walton et al., 2024). Borehole-based studies indicate that while most MTCs
59 are mud-rich, some are sand-prone and contain large, sandstone blocks (Wu et al., 2021). Mud-rich
60 MTCs typically exhibit elevated resistivity, P-wave velocity, and density, along with reduced porosity
61 and water content compared to the surrounding strata (Dugan et al., 2012; Wu et al., 2021).
62 Additionally, the lower intervals of mud-rich MTCs are characterized by the highest P-wave velocity
63 and density along with the lowest porosity, representing the most compacted structure named basal
64 shear zone (Wu et al., 2021). In contrast, the internal sand-rich blocks typically exhibit lower P-wave
65 velocity and density, higher porosity and permeability compared to the surrounding matrix (i.e.,
66 debrites), suggesting they are undercompacted and may maintain high reservoir space (Wu et al.,
67 2021). Therefore, MTCs and their associated basal shear zone are considered effective seals for
68 hydrocarbons, while the sand-rich blocks are considered potential reservoirs for hydrocarbon
69 accumulation.

70 Although MTCs are generally considered effective hydrocarbon seals due to their high compaction
71 and low permeability, recent studies have shown that seal failure may occur in specific part of MTCs.
72 For example, fluid escape features such as pockmarks, gas chimneys, and acoustic anomalies are
73 observed within MTCs, indicating vertical fluid migration and local seal failure (Lastras et al., 2004;
74 Noda et al., 2013; Pattier et al., 2013). The apparent contradiction between the compacted, low-
75 permeability nature of MTCs and the observed indicators of fluid migration prompts an important
76 question: when do MTCs serve as effective seals, and what conditions lead to their failure? To address
77 the above questions, we focus on the Songnan Low Uplift region in the Qiongdongnan Basin, South
78 China Sea, where vertically stacked MTCs are interbedded with gas hydrate-bearing layers and have
79 been repeatedly breached by fluid migration (Yang et al., 2013; Kuang et al. 2023). We integrate 3D
80 seismic reflection and well log data to characterize the morphological and petrophysical properties of

81 the MTCs, evaluate their seal integrity based on petrophysical assessment, and ultimately identify the
82 key factors that control their seal integrity.

83 Our results reveal that during MTC emplacement, the lowermost interval is subject to a strain-
84 focusing mechanism known as shear localization. This process typically occurs along the basal
85 interval beneath relatively flat topography and gives rise to a highly deformed band that corresponds
86 to the basal shear zone previously identified by Wu et al. (2021), which plays a key role in controlling
87 the mechanical and sealing behavior of MTCs. However, basal topographic highs, including frontal
88 ramps and remnant blocks, may interrupt shear localization and result in reduced compaction above
89 these structures. Thus, MTCs function as effective seals when shear localization proceeds normally
90 during emplacement, promoting the formation of a continuous basal shear zone. However, this seal
91 integrity can fail when topographic highs disrupt shear localization and interrupt the continuity of the
92 basal shear zone. Understanding the conditions under which MTCs maintain or lose their seal
93 integrity is critical for evaluating subsurface fluid migration pathways, hydrocarbon trap integrity,
94 and gas hydrate system evolution in deep-water basins. These insights also aid in evaluating gas
95 hydrate reservoirs and guiding site selection for future subsea carbon storage.

96 **2 Geological Setting**

97 QDNB is a Cenozoic rift basin characterized by thick Paleogene to Quaternary sediments
98 (6000~12,000 m) situated atop a Mesozoic igneous basement in the northern South China Sea (Huang
99 et al., 2016). Due to regional erosion caused by the uplift of the Tibetan Plateau and the associated
100 East Asia monsoon, substantial volumes of siliceous sediment are transported from the southwestern
101 Yangtze Block through the Red River system with additional sources from eastern Indochina Block
102 and Hainan (Figure 1a; Su et al., 2019).

103 Multiple phases of rifting and post-rift thermal subsidence have shaped the basin, forming a complex
104 network of normal faults and fracture zones (Yang et al., 2022). These faults act as major conduits

105 for vertical fluid migration, as evidenced by the widespread development of gas chimneys and fault-
106 rooted seepage structures (Cartwright & Santamarina, 2015; Kuang et al., 2023; Serov et al., 2023).
107 Focused fluid flow along these faults promotes gas hydrate formation and overpressure buildup within
108 sediments, both of which contribute to reduced slope stability (Chapp et al., 2008; Hustoft et al., 2009;
109 Mountjoy et al., 2014). The interplay between high sedimentation rates, active faulting, and intense
110 fluid activity in the QDNB thus creates favorable conditions for submarine slope failure and the
111 development of MTCs (Chang et al., 2021; Hunt et al., 2013).

112 The study area specifically focuses on the Songnan Low Uplift within the QDNB, which encompasses
113 key zones targeted for gas hydrate exploration in the South China Sea (Figure 1b). Since 2013, the
114 Guangzhou Marine Geological Survey has identified multiple conventional gas fields and gas hydrate
115 reservoirs in the QDNB, underscoring the region's significance in natural hydrocarbon accumulation
116 (Figure 1b). Seismic and well log data suggest that MTCs are widely developed in the Songnan Low
117 Uplift and often occur in close spatial association with gas hydrate-bearing intervals (Kuang et al.,
118 2023; Ren et al., 2024). This spatial configuration implies a possible sealing relationship, where
119 MTCs may serve as low-permeability barriers that help trap upward-migrating free gas and maintain
120 gas hydrate stability beneath them.

121 **3 Data and Methods**

122 **3.1 Seismic data and well log data**

123 We adopt 3D seismic data provided by Guangzhou Marine Geological Survey. The 3D seismic data
124 were collected from the Songnan Low Uplift region in 2018, covering an area of approximately 360
125 km² with water depths ranging from 1,650 to 1,800 m (Figure 1b). The 3D seismic data are post-stack
126 time-migrated and zero-phase processed with positive amplitudes represented by a red and yellow
127 peak and negative amplitudes represented by a blue and grey trough (Figure 2). The 3D seismic
128 surveys have a dominant frequency of 40 Hz and an average seismic velocity of 1,660 m/s near the
129 seabed sediment, which gives an approximate vertical resolution of c. 10 m for the near seabed

130 sediments.

131 The adopted well log data were acquired using Schlumberger tools from four wells (W1, W2, W3,
132 W4), including density, resistivity, neutron, acoustic, nuclear magnetic measurements, and in-situ
133 temperature measurements (Figure 1b). To establish the relationship between depth domain (true
134 vertical depth; TVD) well log data and time domain (two-way traveltime; TWT) seismic data,
135 seismic-well tie is performed respectively for each well. Seismic-well tie begins with creating a
136 synthetic seismogram using sonic and density logs to simulate how seismic waves travel through
137 subsurface geobodies at the well site (Lines & Newrick, 2004). This synthetic seismogram is then
138 compared to the actual seismic data collected near the well. By aligning the synthetic seismogram
139 with the actual seismic trace, we can ensure that seismic reflections accurately match the geological
140 layers observed in the well, enhancing the reliability of subsurface interpretations (see **Appendix A**
141 for details).

142 **3.2 Seismic attributes analysis**

143 Seismic attributes are quantitative measurements derived from seismic data to reveal subsurface
144 structures and properties that may not be immediately apparent in raw datasets (Chopra & Marfurt,
145 2007). In this study, we use variance and spectral decomposition with RGB blending to enhance the
146 interpretation of complex geological features such as MTCs and fluid escape pipes.

147 The variance attribute measures the variability or heterogeneity within seismic traces, making it ideal
148 for highlighting discontinuities (Chopra & Marfurt, 2007). For MTCs, high variance often
149 corresponds to chaotic zones caused by sediment mixing during transport (Chopra & Marfurt, 2007;
150 Chen et al., 2022). For fluid escape pipes, these features create vertical disturbances in seismic data,
151 which manifest as zones of high variance (Cartwright et al., 2007; Cartwright & Santamarina, 2015).
152 By applying variance attribute, we identify the spatial extent, boundaries, internal architecture of
153 MTCs and enhance the visibility of fluid escape pipes.

154 Spectral decomposition is a frequency based seismic attribute analysis technique that breaks down
155 seismic data into its individual frequency components (Anomneze et al., 2025). RGB blending is a
156 visualization technique that builds on spectral decomposition to create an intuitive representation of
157 frequency content (Bataller et al., 2019). In this method, three narrow frequency bins are split from
158 the decomposed seismic data and assigned to the red (R), green (G), and blue (B) color channels,
159 respectively (Bataller et al., 2019). Areas with similar frequency characteristics then appear in similar
160 colors, allowing us to quickly spot patterns, transitions, or heterogeneities, such as intra-MTCs
161 structures or fluid escape pipes (Eckersley et al., 2018).

162 **3.3 Permeability calculation**

163 Permeability represents a direct quantitative indicator for evaluating seal integrity (Schowalter, 1979).
164 However, in situ measurements of permeability in fine-grained MTCs are difficult and costly to
165 perform. To yield accurate permeability estimation for MTCs, we calculate the permeability from
166 nuclear magnetic resonance measurements through empirical Schlumberger-Doll Research equation
167 developed by Kenyon et al. (1988):

$$168 \quad k = A\phi^4(T_{2LM})^2 \quad (1)$$

169 where $\phi [m^3 \cdot m^{-3}]$ is the porosity, $T_{2LM} [ms]$ is the logarithmic mean of the T_2 distribution, and A
170 $[m^2 \cdot m^{-2}]$ is the fitting coefficient.

171 The investigated MTCs here exhibit elevated clay content (Kuang et al., 2023). For the determination
172 of fitting coefficient a , we implement the function of lithology developed by Daigle and Dugan (2009)
173 specifically for silt- and clay-rich sediments:

$$174 \quad A = -2.7 \times 10^{-18}GR + 2.4 \times 10^{-16} \quad (2)$$

175 where $GR [gAPI]$ is the gamma ray log value.

3.4 Numerical modelling

To approximate the shear deformation within MTCs flowing over topographically variable strata, we implement a two-dimensional numerical solver based on implicit pseudo-transient methods and finite difference discretization (Räss et al., 2022; Liu et al., 2024). We describe failing MTCs as an incompressible, nonlinear, viscous fluid (Iverson, 1997). Under these assumptions, the momentum equations at steady state can be simplified to:

$$\frac{\partial \tau_{ij}}{\partial x_j} - \frac{\partial p}{\partial x_i} + F_i - \rho \left(u_j \frac{\partial u_i}{\partial x_j} \right) = 0 \quad (3)$$

where τ_{ij} [Pa] is the deviatoric stress tensor, p [Pa] is the isotropic pressure, $F_i = \rho g (\sin \alpha, \cos \alpha)$ [$kg \cdot s^{-2} \cdot m^{-2}$] is the gravitational body force at a tilted angle α , $u_j \frac{\partial u_i}{\partial x_j}$ [$m \cdot s^{-2}$] is the convective acceleration term, and $i \in \{x, z\}$ indexes the two spatial components.

Herein, we describe failing sediments as fluid with Herschel-Bulkley rheology behavior. Failing sediments behave as a fluid (i.e., $\tau > \tau_0$), thus neglecting the state of rigid solid. The rheology model for simple shear is implemented using:

$$\tau_{ij} = \tau_0 + k_0 \dot{\epsilon}_{ij}^n \quad (4)$$

where τ_0 is the yield shear stress [Pa], k_0 is the consistency index [$Pa \cdot s^n$], n is the flow index [dimensionless]. The key physical parameters of modelled fluid can be found in Table 1.

Failing sediments flow into the domain from the left boundary over undeforming strata and exits at the right boundary. The analytical inflow field is calculated by solving the momentum balance along the flow at steady state. The outlet boundary condition is following the approach of Kreiss (1968), Gustafsson et al. (1972), and Orlanski (1976).

To prescribe the interface between MTCs and undeformed strata, we implement the immersed-

197 boundary method, a fictitious domain method that allows us to treat fluid and solid domains separately
198 and efficiently (Peskin, 1972, 2002). This method facilitates the independent and computationally
199 efficient handling of fluid and solid domains, making it well-suited for addressing the intricate
200 geometries and dynamic interactions prevalent in MTCs (Peskin, 1972, 2002; Zhao et al., 2021).

201 The detailed explanations of numerical simulation considering pseudo-transient methods, rheology
202 model generalization, boundary conditions, and immersed-boundary method can be accessed in
203 **Appendix B.**

204 **4 Results**

205 In seismic sections, three MTCs are characterized by internally chaotic seismic facies (Figure 2).
206 They are bounded by a continuous high-amplitude basal shear surface and a rugose low-amplitude
207 top surface (Figure 2). These seismic characteristics indicate that three MTCs underwent intensive
208 internal deformation and are categorized as debris-flow type MTCs (Jackson, 2011; Ortiz-Karpf et
209 al., 2017). We pick six horizons defining the bases and tops of three MTCs for seismic attribute and
210 well log analysis (Figure 2).

211 **4.1 MTC-1**

212 **Observation:** MTC-1 is bounded by horizon H1 at its base and horizon H2 at its top (Figure 2). The
213 lateral and distal boundaries of MTC-1 extend beyond the limits of the 3D seismic dataset. Structure
214 map and variance attribute map from horizon H1 shows a series of E-trending lineations that are
215 generally oriented downslope (Figure 3a & b). These lineations range from 50~100m in width,
216 2.5~5.0km in length, and exhibit erosional characteristics, cutting downward into the underlying
217 substrate. The central region of MTC-1 contains a block-shaped feature and exhibits a higher-variance
218 boundary compared to the surrounding area (Figures 3a & b). In the correlated seismic section, the
219 block exhibits internally sub-parallel, continuous, high-amplitude seismic reflections (Figure 2).
220 Below the block, the seismic reflections are marked by high-amplitude and negative polarity opposite

221 to the seabed reflection (Figure 2). Within the blocks, pull-up reflections that vertically traverse the
222 block and overlying MTC-1 (Figure 2). These pull-up seismic reflections form pipe like features
223 extending to the seabed, where they generate 200~500m wide depressions on the seabed (Figure 2).
224 The eastern region of MTC-1 shows a continuous SSW-trending scarp (Figure 3a). In the correlated
225 seismic section, the scarp manifests as a segment of the basal shear surface that discordantly cuts up
226 to a stratigraphically higher strata at a high angle (Figure 2). Spectral decomposition attribute
227 extracted from horizon H1 shows a series of concave-eastward, regularly spaced subparallel
228 lineations developed adjacent to the easternmost part of the scarp (Figure 3c). These subparallel
229 lineations appear in seismic section as semicontinuous, medium-amplitude reflections (Figure 2).

230 **Interpretation:** The E-trending lineations are interpreted as grooves, forming by clasts entrained
231 within the host flow (e.g., debris flow) that abraded the contemporaneous seabed (Figure 3d;
232 Posamentier and Martinsen, 2011; Sobiesiak et al., 2018). Grooves typically develop parallel to the
233 main flow direction, suggesting that MTC-1 was emplaced in a E-direction (Bull et al., 2009). The
234 block-shaped feature, characterized by internally sub-parallel, continuous seismic reflections, is
235 interpreted as a remnant block, representing an isolated segment of sediment that has not undergone
236 failure (Bull et al., 2009). The high-amplitude negative reflections stacked below the remnant block
237 are interpreted as evidence of gas hydrate presence (BSR 3 in Figure 2; Kuang et al., 2023; Wang et
238 al., 2025). We therefore indicate the formation of remnant block is attributed to gas hydrate
239 cementation, which significantly increases sediment strength and inhibits deformation (Zhao et al.,
240 2023).

241 The pull-up seismic reflections with pipe-like geometries are interpreted as manifestations of fluid
242 escape structures (Wang et al., 2025). The updip parts of these pipes, which connect to seabed
243 depressions, are interpreted as pockmarks in previous studies and are indicative of recurrent cold seep
244 activity (Ye et al., 2019; Ren et al., 2024; Wang et al., 2025). Considering the spatial correlation
245 between fluid escape structures that crosscut MTC-1, we infer that seal failure has occurred at the

246 location of the remnant block.

247 The SSW-trending scarp is interpreted as a frontal ramp, formed by the upward incision of the MTCs
248 into shallower stratigraphic levels (Bull et al., 2009). Previous studies indicate that the strata below
249 the frontal ramp are deposited as sandy turbidite complexes (Figure 2; Kuang et al., 2023). The sandy
250 turbidites potentially enhance the mechanical strength thus erosion resistance by raising critical shear
251 stress threshold, thereby promoting the formation of a stepped frontal ramp (Mitchener & Torfs,
252 1996). The concave-eastward, regularly spaced subparallel lineations are interpreted as pressure
253 ridges, formed by a combination of shear compression and resistance from the undeformed sediments
254 during the deceleration and eventual cessation of MTC movement (Figure 3d; Bull et al., 2009).

255 **4.2 MTCs 2&3**

256 **Observation:** MTC-2 is bounded by Horizon H3 at its base and Horizon H4 at its top (Figure 2). Its
257 lateral extent surpasses the limits of the available 3D seismic dataset. Variance and spectral
258 decomposition attributes extracted from the basal shear surface (H3) reveal a series of E-trending
259 lineations, morphologically comparable to those on Horizon H1 (Figures 4a–4c). These lineations
260 terminate at the distal edge of MTC-2, defining a distinct boundary that marks the downslope limit
261 of the MTC-2 (Figures 4b & 4c).

262 MTC-3 is confined between Horizon H5 at the base and Horizon H6 at the top (Figure 2). Its lateral
263 margin extends beyond the 3D seismic dataset. Variance and spectral decomposition attributes from
264 Horizon H5 reveal a basal shear surface characterized by E-trending lineations, ranging from 0.1~2.5
265 km in width and 2.5~15 km in length (Figure 5a–5c). These E-trending lineations exhibit a divergent
266 pattern downslope, suggesting flow spreading and possible lateral unconfined emplacement (Figure
267 5c). The termination of these grooves delineates the distal margin of MTC-3, marked by a distinct
268 boundary of seismic striation cessation (Figures 5b & 5c).

269 A cluster of semi-rounded, crater-like depressions measuring 50~100 m in diameter is observed

beyond the distal margins of MTC-2 and MTC-3 (Figures 4b & 5b). In the variance attribute map, they correspond to zones of elevated variance (Figure 6a), while the spectral decomposition map shows scattered bright spots coinciding with their locations (Figure 6b). In seismic sections, the depressions are situated directly above topographic highs associated with frontal ramp beneath MTC-1 (Figures 6c & 6d). They are bounded by near-vertical ($\sim 90^\circ$) discontinuities but lack internal deformation typically linked to MTCs emplacement, such as folding or faulting.

Interpretation: Consistent with MTC-1, the E-trending lineations on the basal shear surface of MTC-2 and MTC-3 are interpreted as grooves (Figure 4d & 5d; Posamentier and Martinsen, 2011; Sobiesiak et al., 2018). The E-trending erosional features with divergent shape on the basal shear surface of MTC-3 are interpreted as scours, formed when the basal drag is great enough to allow the mass movement to plough into the substrate (Figure 5d; Sobiesiak et al., 2018). Considering the kinematic indicators provided by grooves and scours, the emplacement direction of MTC-2 and MTC-3 is inferred as E-in general.

The semi-rounded, crater-like depressions observed beyond the distal margins of MTC-2 and MTC-3 suggest a post-emplacement origin, likely associated with vertical fluid escape (Figure 6d). Additionally, an exploration well drilled near the fluid escape pipes was halted due to significant influx of methane gas from the borehole, confirming the escaping fluids were methane-bearing (Kuang et al., 2023). The semi-rounded, crater-like depressions are thus interpreted as fluid escape pipes caused by the seepage of methane-bearing fluids (Figure 6d; Cartwright & Santamarina, 2015; Ye et al., 2019). The presence of fluid escape pipes directly above the frontal ramp of MTC-1 (Figure 6d) suggests that seal failure occurred at the frontal ramp crest.

4.3 MTCs petrophysical properties

Observation: Compared to the overlying and underlying non-MTCs units, MTCs are normally characterized by increased density ($1.8\sim 2.0\text{ g/cm}^3$), resistivity ($1.3\sim 2.5\text{ }\Omega\cdot\text{m}$), and decreased porosity

(45~65%), permeability (0.5~6.5 mD), which remains consistent with previously published studies (Figure 7; Dugan, 2012; Sawyer et al., 2009). Within MTC-1, petrophysical properties change sharply across the remnant block and frontal ramp, both of which are topographic highs along the basal shear surface. Above the topographic highs, MTC-1 exhibits lower density (1.6~1.7 g/cm³), lower resistivity (0.7~1.6 $\Omega\cdot\text{m}$), and higher porosity (55~80%) and permeability (2.5~10.5 mD) compared to the normal MTC-1 intervals devoid of these features (Figure 8). More specifically, the density of MTC-1 overlying topographic highs is approximately 13% lower than that of flat areas (Figure 8a), while resistivity decreases by ~39% (Figure 8b), porosity increases by ~23% (Figure 8c), and permeability increases by ~217% (Figure 8d).

Interpretation: The significantly lower density and resistivity, coupled with higher porosity and permeability observed above the remnant block and frontal ramp, indicate a substantially reduced degree of compaction over these topographic highs. The reduced compaction above the remnant block and frontal ramp implies that the seal integrity of MTC-1 in these zones is significantly weakened. This is consistent with the fluid escape structures observed within the remnant block and above frontal ramp, suggesting potential vertical fluid migration pathways (Figure 2 & Figure 6). Thus, the seal integrity of MTC-1 exhibits spatial variability, with the areas above the remnant block and frontal ramp showing lower degrees of compaction and potentially reduced seal integrity.

5 Discussions and Implications

5.1 Shear Localization as a Key Control on MTCs Seal Integrity

Previous studies have identified two primary mechanisms responsible for MTC seal failure: (1) fault-controlled fluid migration, where normal or thrust faults provide permeable pathways for fluid escape (e.g., Pattier et al., 2013; Yang et al., 2013); and (2) overpressure-driven breaching, where MTCs emplacement induces overpressure in underlying strata, triggering upward fluid migration and seal failure (e.g., Moernaut et al., 2017). In this study, the three MTCs exhibit no seismically resolvable internal faulting or folding, and no evidence of overpressure is observed in the underlying gas hydrate

319 system (Kuang et al., 2023), suggesting that neither fault-assisted nor overpressure-driven
320 mechanisms can account for the observed seal failure. The following section investigates the potential
321 triggers of MTCs seal failure in the study area.

322 We use a two-dimensional numerical solver based on finite difference discretization and implicit
323 pseudo-transient methods to model the distribution and evolution of shear strain during MTCs
324 emplacement (Räss et al., 2022; Trujillo-Vela et al., 2022). Numerical simulation shows that, under
325 conditions of flat basal shear surface with a tilt angle 1.2° , shear strain consistently develops within
326 a 4.0~8.0, representing approximately 10~20% of the total MTC thickness confined to its lowermost
327 part (Figure 9a). This concentration of shear strain is referred to as shear localization, characterized
328 by a distinct deformation band with elevated shear strain rates during MTCs emplacement (Anders et
329 al., 2000; Mitchell et al., 2015; Viesca & Rice, 2012). The presence of shear localization in the lower
330 part of the MTC is consistent with petrophysical and outcrop-based studies, which identify the
331 lowermost 15~30 m, accounting for 10~20% MTC total thickness, similar to the modeled proportion,
332 as the densest interval that accommodated the majority of shear deformation during emplacement
333 (Hodgson et al., 2019; Wu et al., 2021).

334 As seismic and well log interpretations reveal that seal failure occurs above the remnant block and
335 frontal ramp, we simulate two additional scenarios in which the MTC basal shear surface traverses
336 these topographic features. In the first scenario, as MTC flows over a frontal ramp, shear strain
337 intensifies along the ramp edge, while it decreases across the ramp crest (Figure 9b). In the second
338 scenario, as the MTC overrides a remnant block, shear strain is elevated along the margins of the
339 basal shear surface adjacent to the block, while it is markedly reduced across the flat upper surface
340 of the block (Figure 9c). These results indicate that as MTCs traverse structures containing positive
341 relief, such as frontal ramps and remnant blocks, the localization of basal shear strain is disrupted,
342 which leads to a decline in shear intensity and a disrupt in the basal shear zone's integrity. This in
343 turn explains the petrophysical observations that MTC intervals above the topographic highs exhibit

344 lower density and resistivity along with higher porosity and permeability, which establishes reduced
345 compaction due to disrupted shear localization as the ultimate cause of MTCs seal failure.

346 Shear strain plays a key role in shaping the microstructure of granular materials, while shear
347 localization influences the spatial distribution of shear strain. High shear strain promotes grain size
348 reduction (Mitchell et al., 2015; Siman-Tov & Brodsky, 2018), collapse of pore bodies (Emmanuel
349 & Day-Stirrat, 2012) and realignment of pore throats (Kanamatsu et al., 2014; Roy et al., 2022; Wang
350 et al., 2020), which collectively reduce permeability and enhance seal integrity (Cardona et al., 2022).
351 In contrast, low shear strain suppresses these effects, allowing partial recovery of pore structures and
352 widening of seepage pathways due to elastic rebound (Zhao et al., 2023). This reduced compaction
353 weakens seal integrity and facilitates fluid escape.

354 In this work, we demonstrate that MTCs seal integrity is primarily controlled by basal topographic
355 variations as they influence the distribution of shear strain through shear localization (Figure 10a).
356 Topographic highs can disrupt the continuity of the shearing and generate localized zones of low
357 shear strain in MTCs. These low-strain regions trigger elastic rebound and limit grain size segregation,
358 which together widen seepage pathways and increase permeability, ultimately weakening the seal
359 integrity of MTCs above such features (Figure 10b). In contrast, flat topography or the margins of
360 topographic highs tend to concentrate shear strain, promoting grain size reduction, pore-throat
361 collapse, and directional pore alignment. These processes restrict fluid migration and enhance the seal
362 integrity of MTCs in these zones (Figure 10c; Gatter et al., 2021).

363 **5.2 Implications for gas hydrate formation and distribution**

364 BSRs in the study area exhibit distinct fluid migration and hydrate formation characteristics, each
365 influenced by the sealing behavior of MTC-1. In regions where MTC-1 maintains an intact basal
366 shear zone (i.e., lacking remnant blocks and frontal ramp), it exhibits strong seal integrity, allowing
367 methane-rich fluids sourced from the Songnan Low Uplift to accumulate beneath the MTC and thus

368 forming BSR 1 (Table 2; Figure 11; Kuang et al., 2023). The free gas associated with BSR 1
369 subsequently migrates laterally, serving as the methane source for the formation of both BSR 2 and
370 BSR 3 (Figure 11).

371 BSR 2 lies beneath an area where MTC-1 also lacks topographic highs and maintains strong seal
372 integrity. The strong seal integrity promotes high-pressure and low-temperature conditions, under
373 which gas hydrate tends to crystallize from methane-rich fluids (Sloan, 2003; Walsh et al., 2009;
374 Crutchley et al., 2014) and eventually leads to the formation of high-saturation gas hydrates in BSR
375 2 (Table 2; Figure 11). However, upon reaching the crest of frontal ramp, where the seal integrity of
376 MTC-1 is compromised, methane-rich fluids are able to migrate vertically. This upward migration
377 penetrates the under-compacted zones in MTC-1 and the overlying MTCs 2&3, resulting in the
378 formation of crater-like pockmarks that serve as geomorphic evidence of focused fluid escape (Figure
379 11).

380 In contrast, BSR 3 lies beneath an area where MTC-1 contains a remnant block and exhibits
381 compromised seal integrity (Figure 11). The weakened seal promotes moderate-pressure and low-
382 temperature conditions, under which methane-rich fluids partially crystallize to gas hydrate during
383 advection and partially remain as free gas (Ker et al., 2019; Milkov et al., 2004; Ruppel & Kessler,
384 2017). This leads to the formation of the low-saturation gas hydrates that coexist with free gas in BSR
385 3 (Table 2; Figure 11). The remained free gas subsequently ascends through the under-compacted
386 zones overlying remnant block and eventually breaches the seabed, forming a cluster of pockmarks
387 (Figure 11).

388 Thus, we demonstrate that the seal integrity of MTCs fundamentally controls fluid migration and
389 hydrate accumulation modes. When MTCs exhibit intact basal shear zone (e.g., lacking frontal ramp
390 or remnant block), they act as effective seals and promote lateral fluid migration, allowing free gas
391 reservoirs (e.g., BSR 1) or high-saturation hydrates (e.g., BSR 2) to form under respectively favorable

392 pressure-temperature conditions. In contrast, when MTCs exhibit disrupted basal shear zone (e.g.,
393 containing frontal ramp or remnant block), the seal integrity of MTCs is compromised. The free gas
394 may migrate vertically through these zones with compromised seal integrity, forming pockmarks
395 when gas supply is limited or coexisting free gas and low-saturation gas hydrates (e.g., BSR 3) when
396 gas supply is sufficient. Therefore, the spatial variability in MTCs seal integrity controls fluid
397 migration pathways, directly governing gas hydrate formation and distribution.

398 **6 Conclusions**

399 In this study, we integrate 3D seismic reflection and well log data to investigate the sealing behavior
400 of three vertically stacked MTCs in the Qiongdongnan Basin, northern South China Sea, with the aim
401 of identifying the key factors that control their seal integrity. We show that:

402 (1) Shear localization consistently develops in the lowermost part of MTCs during emplacement,
403 forming a narrow, highly deformed basal shear zone. This shear-focused deformation enhances
404 compaction, reduces porosity and permeability, and is therefore critical for the seal integrity of MTCs.

405 (2) Topographic highs on basal shear surface such as frontal ramps and remnant blocks can disturb
406 shear localization by reducing localized shear strain. This disruption results in lower degrees of
407 compaction and higher permeability above these topographic highs, ultimately leading to localized
408 seal failure.

409 (3) Shear localization plays a key role in focusing fluid escape and thus governs the spatial distribution
410 and accumulation of gas hydrates. Intact MTC seals promote free gas or high-saturation hydrate
411 accumulation, whereas compromised seals result in low-saturation hydrates coexisting with free gas.

412 (4) Understanding the conditions under which MTCs function as effective seals, or fail, is crucial for
413 predicting gas hydrate distribution and identifying suitable sites for subsea carbon dioxide storage in
414 submarine settings. Therefore, such knowledge of subsurface fluid flow is critical for derisking future
415 hydrocarbon exploration and carbon dioxide storage initiatives.

416 **Appendix A: Seismic well tie**

417 We show one example of seismic-well tie using W1 (Figure A1). Here, sonic and density logs are
418 used to generate synthetic seismograms:

$$419 \quad \text{Reflection} = \frac{\rho_2 v_2 - \rho_1 v_1}{\rho_2 v_2 + \rho_1 v_1} \quad (\text{A1})$$

420 where ρ is density [$kg \cdot m^{-3}$], v is P-wave velocity [$m \cdot s^{-1}$], and the subscripts denote two
421 subsurface layers.

422 The set of reflection coefficients is then band limited to the same frequency band as the actual seismic
423 data (Lines & Newrick, 2004). Between the well log synthetic seismograms and actual seismic data,
424 correlations are made through the vertical stretch or squeeze of the seismograms to match key
425 subsurface intervals. Finally, the relationship between depth domain well log data and time domain
426 seismic data can be established.

427 **Appendix B: Numerical modelling**

428 **B1. Implicit pseudo-transient methods**

429 The implicit pseudo-transient method is a powerful numerical technique renowned for its robustness
430 in tackling strongly nonlinear problems, such as shear band formation in visco-elasto-plastic media
431 (Räss et al., 2022). This iterative approach enhances stability in the solution process by introducing a
432 pseudo-time derivative, making it highly effective for modeling complex rheological behaviors (Räss
433 et al., 2022). Studies have shown it can deliver over 96% parallel efficiency on distributed-memory
434 systems utilizing up to 2197 graphics processing units (Räss et al., 2022). Under these circumstances,
435 implicit pseudo-transient method possesses high robustness and scalability, which makes it well
436 suited for solving the momentum equation to approximate the shear deformation within MTCs.

437 At each physical time step, implicit pseudo-transient method is implemented for the iterative solution
438 to the momentum equation:

$$\frac{\partial p}{\partial \Gamma_p} = -\frac{\partial u_i}{\partial x_i} \quad (B1)$$

$$\frac{\partial u_i}{\partial \Gamma_u} = \frac{\partial \tau_{ij}}{\partial x_j} - \frac{\partial p}{\partial x_i} + F_i - \rho \left(u_j \frac{\partial u_i}{\partial x_j} \right) \quad (B2)$$

where Γ presents the pseudo-time step.

An implicit solution of the momentum equations can be achieved when the continuity residual $\frac{\partial p}{\partial \Gamma_p}$ and the momentum residual $\frac{\partial u_i}{\partial \Gamma_u}$ are minimized. The detailed implementation processes of implicit pseudo-transient methods can be found in Räss et al. (2022).

B2. Herschel-Bulkley rheology model

The generalized rheology model for simple shear is implemented using:

$$\tau_{ij} = \tau_0 + k_0 \dot{\epsilon}_{ij}^n \quad (B3)$$

$$\left| \frac{\dot{\epsilon}_{ij}}{\dot{\epsilon}_r} \right|^n = \text{sgn}(\dot{\epsilon}_{ij}) \frac{\tau_{ij}}{\tau_0} - 1 \quad (B4)$$

where τ_0 is the yield shear stress [Pa], k_0 is the consistency index [Pa · sⁿ], n is the flow index [dimensionless], $\dot{\epsilon}_{ij}$ is the strain rate tensor [s⁻¹], given as:

$$\dot{\epsilon}_{ij} = \sqrt{\frac{1}{2} \tau_{ij} \tau_{ij}} \quad (B5)$$

$\dot{\epsilon}_r$ is the reference strain rate [s⁻¹], given as:

$$\dot{\epsilon}_r = \left(\frac{\tau_0}{k_0} \right)^{\frac{1}{n}} \quad (B6)$$

The detailed implementation processes can be found in Zafar et al. (2024).

B3. Outlet boundary conditions

We adopt the outlet boundary condition from Orlanski (1976). This boundary condition allows phenomena generated in the domain of interest to pass through the boundary without undergoing significant distortion or influencing the interior solution, and it is an optimal solution for balancing accuracy and efficiency.

$$\frac{\partial u}{\partial t} + U \frac{\partial u}{\partial x} = 0 \quad (\text{B7})$$

From Kreiss (1968) and Gustafsson et al. (1972), the propagation speed U is numerically estimated by $U = \frac{\Delta x}{\Delta t}$, where Δx and Δt are the spatial and temporal grid sizes. The speed at the outlet boundary is then as follows:

$$u_{n_x}^{n_t} = 2u_{n_x-1}^{n_{t-1}} - u_{n_x-2}^{n_{t-2}} \quad (\text{B8})$$

where n_x is the boundary point and n_t is the current time step.

B4. Immersed-boundary method

Immersed-boundary method is used to prescribe the fictitious interface between MTCs and undeformed strata. The general idea is using both Eulerian and Lagrangian approaches to solve the governing equations on the MTC domain with a correction on the interface between MTCs and undeformed strata (Zhao et al., 2021). Lagrangian approach describes fluid motion focusing on an individual fluid parcel as it moves through space and time, while Eulerian approach describes fluid motion focusing on specific locations in the space through which the fluid flows as time passes (Peskin, 1972, 2002). The interface (the immersed boundary) is represented independently as a set of discrete points (Lagrangian variables) that define its shape and position (Peskin, 1972, 2002). This interface cuts through the MTC domain grid (Eulerian variables), which is the fixed grid where the governing equations are solved (Peskin, 1972, 2002). This method avoids the computationally expensive and often challenging task of generating and deforming body-conforming meshes for

intricate or rapidly moving boundaries (e.g. basal shear surface). The detailed implementation processes of the immersed-boundary method can be found in Zhao et al. (2021) and Liu et al. (2024).

Appendix C: Gas hydrate saturation estimation

To determine the actual formations of multiple amplitude anomalies in seismic data, gas hydrate saturation is calculated using Archie's porosity-resistivity equation and saturation equation (Archie, 1942):

$$S_h = 1 - \left(\frac{R_0}{R_m} \right)^{\frac{1}{n_{Archie}}}, \quad R_0 = \frac{R_w}{\phi^m} \quad (C1)$$

where S_h [$m^3 \cdot ms^{-3}$] is the gas hydrate saturation, R_0 [Ω_m] is the background resistivity, R_m [Ω_m] is the measured resistivity, n_{Archie} [dimensionless] is Archie's saturation exponent (set equal to 2.5 according to Cook and Waite, 2018), R_w [Ω_m] is the pore water resistivity (set equal to $0.3\Omega_m$ according to the resistivity of seawater), m is the cementation exponent (set equal to 2 according to Cook et al., 2023).

Acknowledgments

We thank the Guangzhou Marine Geological Survey for providing seismic and well log data and for granting permission to publish this work. This research was supported by the National Key Research and Development Program of China (Grant No. 2021YFC2800901). The corresponding author also acknowledges financial support from the National Natural Science Foundation of China (Grant No. 42406060), the Natural Science Foundation of Shanghai (Grant No. 23ZR1467800), and the Fundamental Research Funds for the Central Universities, China.

Data Availability Statement

The 3D seismic and well log data were obtained from a series of proprietary surveys conducted by the Guangzhou Marine Geological Survey in 2018, 2021 and 2022 for the gas hydrate exploration. These data, uploaded by Kuang et al. (2023), are available in the Zenodo repository

501 (<https://doi.org/10.5281/zenodo.7721790>). The codes used for numerical simulations are available in
502 the Zenodo repository (<https://zenodo.org/records/16252096>). Requests for datasets can be made
503 through Guangzhou Marine Geological Survey via the corresponding author.

504 **References**

- 505 Alves, T. M., & Cartwright, J. A. (2010). The effect of mass-transport deposits on the younger slope
506 morphology, offshore Brazil. *Marine and Petroleum Geology*, 27(9), 2027–2036.
507 <https://doi.org/10.1016/j.marpetgeo.2010.05.006>
- 508 Alves, T. M., Kurtev, K., Moore, G. F., & Strasser, M. (2014). Assessing the internal character,
509 reservoir potential, and seal competence of mass-transport deposits using seismic texture: A
510 geophysical and petrophysical approach. *AAPG Bulletin*, 98(4), 793–824.
511 <https://doi.org/10.1306/09121313117>
- 512 Anders, M. H., Aharonov, E., & Walsh, J. J. (2000). Stratified granular media beneath large slide
513 blocks: Implications for mode of emplacement. *Geology*, 28(11), 971–974.
514 [https://doi.org/10.1130/0091-7613\(2000\)28<971:SGMBLS>2.0.CO;2](https://doi.org/10.1130/0091-7613(2000)28<971:SGMBLS>2.0.CO;2)
- 515 Anomneze, D. O., Oguadinma, V. O., Ayodele, I. J., & Ajaegwu, N. E. (2025). Application of iso-
516 frequency extractions and spectral frequency blending in hydrocarbon delineation of thin-pay
517 and thick-pay reservoirs, Niger Delta Basin. *Energy Geoscience*, 6(2), 100396.
518 <https://doi.org/10.1016/j.engeos.2025.100396>
- 519 Archie, G. E. (1942). The Electrical Resistivity Log as an Aid in Determining Some Reservoir
520 Characteristics. *Transactions of the AIME*, 146(01), 54–62. [https://doi.org/10.2118/942054-](https://doi.org/10.2118/942054-G)
521 [G](https://doi.org/10.2118/942054-G)
- 522 Bataller, F. J., McDougall, N., & Moscariello, A. (2019). Ordovician glacial paleogeography:
523 Integration of seismic spectral decomposition, well sedimentological data, and glacial modern
524 analogs in the Murzuq Basin, Libya. *Interpretation*, 7(2), T383–T408.
525 <https://doi.org/10.1190/INT-2018-0069.1>
- 526 Bull, S., Cartwright, J., & Huuse, M. (2009). A review of kinematic indicators from mass-transport
527 complexes using 3D seismic data. *Marine and Petroleum Geology*, 26(7), 1132–1151.
528 <https://doi.org/10.1016/j.marpetgeo.2008.09.011>
- 529 Cardona, S., Kobayashi, H., Wood, L., Dugan, B., & Milkov, A. V. (2022). Assessing the sealing
530 quality of submarine mass transport complexes and deposits. *Marine and Petroleum Geology*,
531 143, 105748. <https://doi.org/10.1016/j.marpetgeo.2022.105748>
- 532 Cartwright, J., Huuse, M., & Aplin, A. (2007). Seal bypass systems. *AAPG bulletin*, 91(8), 1141-
533 1166.
- 534 Cartwright, J., & Santamarina, C. (2015). Seismic characteristics of fluid escape pipes in sedimentary
535 basins: Implications for pipe genesis. *Marine and Petroleum Geology*, 65, 126-140.
- 536 Chang, Y.-C., Mitchell, N. C., & Quartau, R. (2021). Landslides in the Upper Submarine Slopes of
537 Volcanic Islands: The Central Azores. *Geochemistry, Geophysics, Geosystems*, 22(10),
538 e2021GC009833. <https://doi.org/10.1029/2021GC009833>
- 539 Chapp, E., Taylor, B., Oakley, A., & Moore, G. F. (2008). A seismic stratigraphic analysis of Mariana
540 forearc basin evolution. *Geochemistry, Geophysics, Geosystems*, 9(10).
541 <https://doi.org/10.1029/2008GC001998>

542 Chen, D., Zhang, G., Dong, D., Zhao, M., & Wang, X. (2022). Widespread Fluid Seepage Related to
543 Buried Submarine Landslide Deposits in the Northwestern South China Sea. *Geophysical*
544 *Research Letters*, 49(6), e2021GL096584. <https://doi.org/10.1029/2021GL096584>

545 Chopra, S., & Marfurt, K. J. (2007). *Seismic Attributes for Prospect Identification and Reservoir*
546 *Characterization*. Society of Exploration Geophysicists and European Association of
547 Geoscientists and Engineers. <https://doi.org/10.1190/1.9781560801900>

548 Cook, A. E., Portnov, A., Heber, R. C., Vadakkepuliambatta, S., & Bünz, S. (2023). Widespread
549 subseafloor gas hydrate in the Barents Sea and Norwegian Margin. *Earth and Planetary*
550 *Science Letters*, 604, 117993. <https://doi.org/10.1016/j.epsl.2023.117993>

551 Cook, A. E., & Waite, W. F. (2018). Archie's Saturation Exponent for Natural Gas Hydrate in Coarse-
552 Grained Reservoirs. *Journal of Geophysical Research: Solid Earth*, 123(3), 2069–2089.
553 <https://doi.org/10.1002/2017JB015138>

554 Crutchley, G. J., Klaeschen, D., Planert, L., Bialas, J., Berndt, C., Papenberg, C., Hensen, C.,
555 Hornbach, M. J., Krastel, S., & Brueckmann, W. (2014). The impact of fluid advection on gas
556 hydrate stability: Investigations at sites of methane seepage offshore Costa Rica. *Earth and*
557 *Planetary Science Letters*, 401, 95–109. <https://doi.org/10.1016/j.epsl.2014.05.045>

558 Daigle, H., & Dugan, B. (2009). Extending NMR data for permeability estimation in fine-grained
559 sediments. *Marine and Petroleum Geology*, 26(8), 1419–1427.
560 <https://doi.org/10.1016/j.marpetgeo.2009.02.008>

561 Day-Stirrat, R. J., Flemings, P. B., You, Y., & van der Pluijm, B. A. (2013). Modification of mudstone
562 fabric and pore structure as a result of slope failure: Ursa Basin, Gulf of Mexico. *Marine*
563 *Geology*, 341, 58–67. <https://doi.org/10.1016/j.margeo.2013.05.003>

564 Dugan, B. (2012). Petrophysical and consolidation behavior of mass transport deposits from the
565 northern Gulf of Mexico, IODP Expedition 308. *Marine Geology*, 315–318, 98–107.
566 <https://doi.org/10.1016/j.margeo.2012.05.001>

567 Gatter, R., Clare, M. A., Kuhlmann, J., & Huhn, K. (2021). Characterisation of weak layers, physical
568 controls on their global distribution and their role in submarine landslide formation. *Earth-*
569 *Science Reviews*, 223, 103845. <https://doi.org/10.1016/j.earscirev.2021.103845>

570 Gustafsson, B., Kreiss, H.-O., & Sundström, A. (1972). Stability Theory of Difference
571 Approximations for Mixed Initial Boundary Value Problems. II. *Mathematics of Computation*,
572 26(119), 649–686. <https://doi.org/10.2307/2005093>

573 Eckersley, A. J., Lowell, J., & Szafian, P. (2018). High-definition frequency decomposition.
574 *Geophysical Prospecting*, 66(6), 1138–1143. <https://doi.org/10.1111/1365-2478.12642>

575 Emmanuel, S., & Day-Stirrat, R. J. (2012). A framework for quantifying size dependent deformation
576 of nano-scale pores in mudrocks. *Journal of Applied Geophysics*, 86, 29–35.
577 <https://doi.org/10.1016/j.jappgeo.2012.07.011>

578 Han, Z. (2025). Shear localization as a key control on mass-transport complexes seal integrity:
579 insights from geophysical datasets [Dataset]. *Zenodo*. <https://zenodo.org/records/16252096>

580 Hodgson, D. M., Brooks, H. L., Ortiz-Karpf, A., Spychala, Y., Lee, D. R., & Jackson, C. A.-L. (2019).
581 Entrainment and abrasion of megaclasts during submarine landsliding and their impact on
582 flow behaviour. *Geological Society, London, Special Publications*, 477(1), 223–240.
583 <https://doi.org/10.1144/SP477.26>

584 Huang, B., Tian, H., Li, X., Wang, Z., & Xiao, X. (2016). Geochemistry, origin and accumulation of
585 natural gases in the deepwater area of the Qiongdongnan Basin, South China Sea. *Marine and*
586 *Petroleum Geology*, 72, 254–267. <https://doi.org/10.1016/j.marpetgeo.2016.02.007>

- 587 Hunt, J. E., Wynn, R. B., Talling, P. J., & Masson, D. G. (2013). Turbidite record of frequency and
588 source of large volume (>100 km³) Canary Island landslides in the last 1.5 Ma: Implications
589 for landslide triggers and geohazards. *Geochemistry, Geophysics, Geosystems*, 14(7), 2100–
590 2123. <https://doi.org/10.1002/ggge.20139>
- 591 Hustoft, S., Dugan, B., & Mienert, J. (2009). Effects of rapid sedimentation on developing the Nyegga
592 pockmark field: Constraints from hydrological modeling and 3-D seismic data, offshore mid-
593 Norway. *Geochemistry, Geophysics, Geosystems*, 10(6).
594 <https://doi.org/10.1029/2009GC002409>
- 595 Iverson, R. M. (1997). The physics of debris flows. *Reviews of Geophysics*, 35(3), 245–296.
596 <https://doi.org/10.1029/97RG00426>
- 597 Jackson, C. A.-L. (2011). Three-dimensional seismic analysis of megaclast deformation within a mass
598 transport deposit; implications for debris flow kinematics. *Geology*, 39(3), 203–206.
599 <https://doi.org/10.1130/G31767.1>
- 600 Kanamatsu, T., Kawamura, K., Strasser, M., Novak, B., & Kitamura, Y. (2014). Flow dynamics of
601 Nankai Trough submarine landslide inferred from internal deformation using magnetic fabric.
602 *Geochemistry, Geophysics, Geosystems*, 15(10), 4079–4092.
603 <https://doi.org/10.1002/2014GC005409>
- 604 Karstens, J., Haflidason, H., Berndt, C., & Crutchley, G. J. (2023). Revised Storegga Slide
605 reconstruction reveals two major submarine landslides 12,000 years apart. *Communications*
606 *Earth & Environment*, 4(1), 1–9. <https://doi.org/10.1038/s43247-023-00710-y>
- 607 Kenyon, W. E., Day, P. I., Straley, C., & Willemsen, J. F. (1988). A three-part study of NMR
608 longitudinal relaxation properties of water-saturated sandstones. *SPE formation*
609 *evaluation*, 3(03), 622–636.
- 610 Ker, S., Thomas, Y., Riboulot, V., Sultan, N., Bernard, C., Scalabrin, C., Ion, G., & Marsset, B. (2019).
611 Anomalously Deep BSR Related to a Transient State of the Gas Hydrate System in the
612 Western Black Sea. *Geochemistry, Geophysics, Geosystems*, 20(1), 442–459.
613 <https://doi.org/10.1029/2018GC007861>
- 614 Kreiss, H.-O. (1968). Stability Theory for Difference Approximations of Mixed Initial Boundary
615 Value Problems. I. *Mathematics of Computation*, 22(104), 703–714.
616 <https://doi.org/10.2307/2004572>
- 617 Kuang, Z., Cook, A., Ren, J., Deng, W., Cao, Y., & Cai, H. (2023). A Flat-Lying Transitional Free
618 Gas to Gas Hydrate System in a Sand Layer in the Qiongdongnan Basin of the South China
619 Sea. *Geophysical Research Letters*, 50(24), e2023GL105744.
620 <https://doi.org/10.1029/2023GL105744>
- 621 Kuang, Z., Cook, A., Ren, J., Deng, W., Cao, Y., & Cai, H. (2023). A flat-lying transitional free gas
622 to gas hydrate system in a sand layer in the Qiongdongnan Basin of the South China Sea
623 [Dataset]. *Zenodo*. <https://doi.org/10.5281/zenodo.7721790>
- 624 Lastras, G., Canals, M., Urgeles, R., Hughes-Clarke, J. E., & Acosta, J. (2004). Shallow slides and
625 pockmark swarms in the Eivissa Channel, western Mediterranean Sea. *Sedimentology*, 51(4),
626 837–850.
- 627 Lines, L. R., & Newrick, R. T. (2004). *Fundamentals of geophysical interpretation*. Society of
628 Exploration Geophysicists.
- 629 Liu, E. W., Räss, L., Herman, F., Podladchikov, Y., & Suckale, J. (2024). Spontaneous Formation of
630 an Internal Shear Band in Ice Flowing Over Topographically Variable Bedrock. *Journal of*

631 *Geophysical Research: Earth Surface*, 129(4), e2022JF007040.
632 <https://doi.org/10.1029/2022JF007040>

633 Milkov, A. V., Dickens, G. R., Claypool, G. E., Lee, Y.-J., Borowski, W. S., Torres, M. E., Xu, W.,
634 Tomaru, H., Tréhu, A. M., & Schultheiss, P. (2004). Co-existence of gas hydrate, free gas,
635 and brine within the regional gas hydrate stability zone at Hydrate Ridge (Oregon margin):
636 Evidence from prolonged degassing of a pressurized core. *Earth and Planetary Science*
637 *Letters*, 222(3), 829–843. <https://doi.org/10.1016/j.epsl.2004.03.028>

638 Mitchell, T. M., Smith, S. A. F., Anders, M. H., Di Toro, G., Nielsen, S., Cavallo, A., & Beard, A. D.
639 (2015). Catastrophic emplacement of giant landslides aided by thermal decomposition: Heart
640 Mountain, Wyoming. *Earth and Planetary Science Letters*, 411, 199–207.
641 <https://doi.org/10.1016/j.epsl.2014.10.051>

642 Mitchener, H., & Torfs, H. (1996). Erosion of mud/sand mixtures. *Coastal Engineering*, 29(1), 1–25.
643 [https://doi.org/10.1016/S0378-3839\(96\)00002-6](https://doi.org/10.1016/S0378-3839(96)00002-6)

644 Moernaut, J., Wiemer, G., Reusch, A., Stark, N., De Batist, M., Urrutia, R., Ladrón de Guevara, B.,
645 Kopf, A., & Strasser, M. (2017). The influence of overpressure and focused fluid flow on
646 subaquatic slope stability in a formerly glaciated basin: Lake Villarrica (South-Central Chile).
647 *Marine Geology*, 383, 35–54. <https://doi.org/10.1016/j.margeo.2016.11.012>

648 Mountjoy, J. J., Pecher, I., Henrys, S., Crutchley, G., Barnes, P. M., & Plaza-Faverola, A. (2014).
649 Shallow methane hydrate system controls ongoing, downslope sediment transport in a low-
650 velocity active submarine landslide complex, Hikurangi Margin, New Zealand. *Geochemistry,*
651 *Geophysics, Geosystems*, 15(11), 4137–4156. <https://doi.org/10.1002/2014GC005379>

652 Noda, A., TuZino, T., Joshima, M., & Goto, S. (2013). Mass transport-dominated sedimentation in a
653 foreland basin, the Hidaka Trough, northern Japan. *Geochemistry, Geophysics, Geosystems*,
654 14(8), 2638–2660. <https://doi.org/10.1002/ggge.20169>

655 Orlanski, I. (1976). A simple boundary condition for unbounded hyperbolic flows. *Journal of*
656 *computational physics*, 21(3), 251-269.

657 Ortiz-Karpf, A., Hodgson, D. M., Jackson, C. A.-L., & McCaffrey, William. D. (2017). Influence of
658 Seabed Morphology and Substrate Composition On Mass-Transport Flow Processes and
659 Pathways: Insights From the Magdalena Fan, Offshore Colombia. *Journal of Sedimentary*
660 *Research*, 87(3), 189–209. <https://doi.org/10.2110/jsr.2017.10>

661 Pattier, F., Loncke, L., Gaullier, V., Basile, C., Maillard, A., Imbert, P., Roest, W. R., Vendeville, B.
662 C., Patriat, M., & Loubrieu, B. (2013). Mass-transport deposits and fluid venting in a
663 transform margin setting, the eastern Demerara Plateau (French Guiana). *Marine and*
664 *Petroleum Geology*, 46, 287–303. <https://doi.org/10.1016/j.marpetgeo.2013.06.010>

665 Peskin, C. S. (1972). Flow patterns around heart valves: a numerical method. *Journal of*
666 *computational physics*, 10(2), 252-271.

667 Peskin, C. S. (2002). The immersed boundary method. *Acta numerica*, 11, 479-517.

668 Posamentier, H. W., & Martinsen, O. J. (2011). The character and genesis of submarine mass-
669 transport deposits: insights from outcrop and 3D seismic data. Mass-transport deposits in
670 deepwater settings. *Society for Sedimentary Geology (SEPM) Special Publication*, 96, 7-38.

671 Räss, L., Utkin, I., Duretz, T., Omlin, S., & Podladchikov, Y. Y. (2022). Assessing the robustness
672 and scalability of the accelerated pseudo-transient method. *Geoscientific Model Development*,
673 15(14), 5757–5786. <https://doi.org/10.5194/gmd-15-5757-2022>

674 Ren, J., Qiu, H., Kuang, Z., Li, T., He, Y., Xu, M., Wang, X., Lai, H., & Liang, J. (2024). Deep-large
675 faults controlling on the distribution of the venting gas hydrate system in the middle of the

676 Qiongdongnan Basin, South China Sea. *China Geology*, 7(1), 36–50.
677 <https://doi.org/10.31035/cg2023086>

678 Roy, N., Frost, J. D., & Viggiani, G. (2022). Pore space evolution of granular assemblies under shear:
679 An experimental study using X-ray tomography. *Granular Matter*, 24(2), 63.

680 Ruppel, C. D., & Kessler, J. D. (2017). The interaction of climate change and methane hydrates.
681 *Reviews of Geophysics*, 55(1), 126–168. <https://doi.org/10.1002/2016RG000534>

682 Sager, T. F., Urlaub, M., Kaminski, P., Papenberg, C., Lastras, G., Canals, M., & Berndt, C. (2022).
683 Development and Emplacement of Ana Slide, Eivissa Channel, Western Mediterranean Sea.
684 *Geochemistry, Geophysics, Geosystems*, 23(11), e2022GC010469.
685 <https://doi.org/10.1029/2022GC010469>

686 Sawyer, D. E., Flemings, P. B., Dugan, B., & Germaine, J. T. (2009). Retrogressive failures recorded
687 in mass transport deposits in the Ursa Basin, Northern Gulf of Mexico. *Journal of Geophysical*
688 *Research: Solid Earth*, 114(B10). <https://doi.org/10.1029/2008JB006159>

689 Schowalter, T. T. (1979). Mechanics of secondary hydrocarbon migration and entrapment. *AAPG*
690 *bulletin*, 63(5), 723–760.

691 Serov, P., Matningsdal, R., Winsborrow, M., Patton, H., & Andreassen, K. (2023). Widespread natural
692 methane and oil leakage from sub-marine Arctic reservoirs. *Nature Communications*, 14(1),
693 1782. <https://doi.org/10.1038/s41467-023-37514-9>

694 Siman-Tov, S., & Brodsky, E. E. (2018). Gravity-Independent Grain Size Segregation in
695 Experimental Granular Shear Flows as a Mechanism of Layer Formation. *Geophysical*
696 *Research Letters*, 45(16), 8136–8144. <https://doi.org/10.1029/2018GL078486>

697 Sloan, E. D. (2003). Fundamental principles and applications of natural gas hydrates. *Nature*,
698 426(6964), 353–359. <https://doi.org/10.1038/nature02135>

699 Sobiesiak, M. S., Kneller, B., Alsop, G. I., & Milana, J. P. (2018). Styles of basal interaction beneath
700 mass transport deposits. *Marine and Petroleum Geology*, 98, 629–639.
701 <https://doi.org/10.1016/j.marpetgeo.2018.08.028>

702 Su, M., Wu, C., Chen, H., Li, D., Jiang, T., Xie, X., Jiao, H., Wang, Z., & Sun, X. (2019). Late
703 Miocene provenance evolution at the head of Central Canyon in the Qiongdongnan Basin,
704 Northern South China Sea. *Marine and Petroleum Geology*, 110, 787–796.
705 <https://doi.org/10.1016/j.marpetgeo.2019.07.053>

706 Talling, P. J., Wynn, R. B., Masson, D. G., Frenz, M., Cronin, B. T., Schiebel, R., Akhmetzhanov, A.
707 M., Dallmeier-Tiessen, S., Benetti, S., Weaver, P. P. E., Georgiopoulou, A., Zühlsdorff, C.,
708 & Amy, L. A. (2007). Onset of submarine debris flow deposition far from original giant
709 landslide. *Nature*, 450(7169), 541–544. <https://doi.org/10.1038/nature06313>

710 Trujillo-Vela, M. G., Ramos-Cañón, A. M., Escobar-Vargas, J. A., & Galindo-Torres, S. A. (2022).
711 An overview of debris-flow mathematical modelling. *Earth-Science Reviews*, 232, 104135.
712 <https://doi.org/10.1016/j.earscirev.2022.104135>

713 Viesca, R. C., & Rice, J. R. (2012). Nucleation of slip-weakening rupture instability in landslides by
714 localized increase of pore pressure. *Journal of Geophysical Research: Solid Earth*, 117(B3).

715 Walsh, M. R., Koh, C. A., Sloan, E. D., Sum, A. K., & Wu, D. T. (2009). Microsecond Simulations
716 of Spontaneous Methane Hydrate Nucleation and Growth. *Science*, 326(5956), 1095–1098.
717 <https://doi.org/10.1126/science.1174010>

718 Walton, M. A. L., Conrad, J. E., Papesh, A. G., Brothers, D. S., Kluesner, J. W., McGann, M., &
719 Dartnell, P. (2024). A Comprehensive Assessment of Submarine Landslides and Mass

720 Wasting Processes Offshore Southern California. *Geochemistry, Geophysics, Geosystems*,
721 25(3), e2023GC011258. <https://doi.org/10.1029/2023GC011258>

722 Wang, X., Wang, W., Jin, J., Zhang, G., Luan, Z., Li, C., Wang, M., Zhang, Z., Liu, B., Li, W., & Li,
723 S. (2025). Multiple observations to delineate the characteristics of cold seep system in the
724 Qiongdongnan Basin. *Marine and Petroleum Geology*, 181, 107522.
725 <https://doi.org/10.1016/j.marpetgeo.2025.107522>

726 Wang, Y., Wang, Y., & Zhang, J. (2020). Connecting shear localization with the long-range
727 correlated polarized stress fields in granular materials. *Nature Communications*, 11(1), 4349.
728 <https://doi.org/10.1038/s41467-020-18217-x>

729 Wu, N., Jackson, C. A.-L., Johnson, H. D., & Hodgson, D. M. (2021). Lithological, petrophysical,
730 and seal properties of mass-transport complexes, northern Gulf of Mexico. *AAPG Bulletin*,
731 105(7), 1461–1489. <https://doi.org/10.1306/06242019056>

732 Yang, G., Yin, H., Gan, J., Wang, W., Zhu, J., Jia, D., Xiong, X., & Xu, W. (2022). Explaining
733 structural difference between the eastern and western zones of the Qiongdongnan Basin,
734 northern South China Sea: Insights from scaled physical models. *Tectonics*, 41(2),
735 e2021TC006899.

736 Yang, J., Davies, R. J., & Huuse, M. (2013). Gas migration below gas hydrates controlled by mass
737 transport complexes, offshore Mauritania. *Marine and Petroleum Geology*, 48, 366–378.
738 <https://doi.org/10.1016/j.marpetgeo.2013.09.003>

739 Ye, J., Wei, J., Liang, J., Lu, J., Lu, H., & Zhang, W. (2019). Complex gas hydrate system in a gas
740 chimney, South China Sea. *Marine and Petroleum Geology*, 104, 29–39.
741 <https://doi.org/10.1016/j.marpetgeo.2019.03.023>

742 Zafar, M. N., Dutykh, D., Sabatier, P., Banjan, M., & Kim, J. (2024). Numerical Reconstruction of
743 Landslide Paleotsunami Using Geological Records in Alpine Lake Aiguebelette. *Journal of*
744 *Geophysical Research: Solid Earth*, 129(5), e2023JB028629.
745 <https://doi.org/10.1029/2023JB028629>

746 Zhao, E., Dong, Y., Tang, Y., & Cui, L. (2021). Numerical study on hydrodynamic load and vibration
747 of pipeline exerted by submarine debris flow. *Ocean Engineering*, 239, 109754.
748 <https://doi.org/10.1016/j.oceaneng.2021.109754>

749 Zhao, Y., Liu, J., Sang, S., Hua, L., Kong, L., Zeng, Z., & Yuan, Q. (2023). Experimental
750 investigation on the permeability characteristics of methane hydrate-bearing clayey-silty
751 sediments considering various factors. *Energy*, 269, 126811.
752 <https://doi.org/10.1016/j.energy.2023.126811>

753 **Table and Figure Captions**

754 Table 1. Parameters and corresponding values for numerical simulation.

755 Table 2. Petrophysical properties of BSRs and associated interpretations.

756 Figure 1. (a) Overview map of the South China Sea showing the boundary of the Qiongdongnan Basin
757 (red polygon). The black box indicates the extent of figure 1b. The arrows indicate the sediment
758 transport directions. (b) Structural units of the Qiongdongnan Basin with locations of the 3D seismic
759 surveys and well log data.

760 Figure 2. Perspective view of seismic volume with cross-wells section A-A' (See Figure 1b for
761 location). The upper surface of the seismic volume is shown as a horizon slice 25ms downwards from
762 seismic horizon H1.

763 Figure 3. (a) Structure map of Horizon H1 illustrating the basal shear surface of MTC-1. (b) Variance
764 attribute extracted along Horizon H1, showing the grooves, remnant block, frontal ramp. (c) Spectral
765 decomposition and associated frequency attribute extracted along Horizon H1, showing the pressure
766 ridges. RGB Blending is applied as 45Hz, 50Hz, and 60Hz. (d) Interpreted sketch of MTC-1, showing
767 its key kinematic indicators and transport direction.

768 Figure 4. (a) Structure map of Horizon H3 illustrating the basal shear surface of MTC-2. (b) Variance
769 attribute extracted along the surface 10ms above Horizon H3, showing the grooves, fluid escape pipes,
770 and boundaries of the MTC-2. (c) Spectral decomposition and associated frequency attributes
771 extracted along Horizon H3, showing the grooves, and boundaries of MTC-2. RGB Blending is
772 applied as 40Hz, 50Hz, and 60Hz. (d) Interpreted sketch of MTC-2, showing its boundaries, key
773 kinematic indicators, and transport direction.

774 Figure 5. (a) Structure map of Horizon H5 illustrating the basal shear surface of MTC-3. (b) Variance
775 attribute extracted along the surface 25ms above Horizon H5, showing the grooves, scours, fluid

776 escape pipes, and boundaries of MTC-3. (c) Spectral decomposition and associated frequency
777 attributes extracted along Horizon H5, showing the scours and boundaries of MTC-3. RGB Blending
778 is applied as 45Hz, 50Hz, and 60Hz. (d) Interpreted sketch of MTC-3, showing its boundaries, key
779 kinematic indicators, and transport direction.

780 Figure 6. (a) Variance horizon slice through the area with semi-rounded, crater-like depressions
781 (25ms above Horizon H5). See Figure 5d for the extent of Figure 6a. (b) Spectral decomposition
782 horizon slice through the area with semi-rounded, crater-like depressions (25ms above Horizon H5).
783 See Figure 5d for the extent of Figure 6b. (c) Uninterpreted seismic section B-B' showing the seismic
784 characteristics of semi-rounded, crater-like depressions. (d) Interpreted sketch of section B-B',
785 showing the high-angle deformation characteristics indicative of fluid escape pipes.

786 Figure 7. Multi-well correlation showing the log responses of MTCs, free gas-bearing sediments, and
787 gas hydrate-bearing sediments. GR: gamma ray; TNPH: thermal neutron porosity; DEN: bulk density;
788 RES_BS: shallow button resistivity; RES_BD: deep button resistivity; V_p : P-wave velocity; Gas Vol:
789 undisturbed zone gas volume fraction; DHAT: downhole annulus temperature. See **Appendix C** for
790 details of hydrate saturation calculations.

791 Figure 8. Petrophysical differences between MTC-1 over flat topography and MTC-1 over
792 topographic highs. (a) density; (b) resistivity; (c) porosity; (d) permeability. The data are retrieved
793 from well log data in the interval between horizon H1 and H2, see Figure 2 and Figure 7 for more
794 details. The depth of color reflects the kernel density which is a measurement of data tendency.

795 Figure 9. Numerical simulation showing shear strain distribution in MTCs under different
796 topographies: (a) flat topography; (b) frontal ramp; (c) remnant block.

797 Figure 10. The role of shear localization in controlling seal integrity of MTCs. (a) Three-dimensional
798 sketch showing the effect of topographic highs on shear localization development; (b) microscopic

799 change of pore structure when shear is weakened; (c) microscopic change of pore structure when
800 shear is strengthened.

801 Figure 11. Three-dimensional schematic diagram showing the methane-bearing fluid migration
802 pathways. Reddish yellow arrows indicate the migration of methane-bearing fluid. The upper surface
803 of the seismic volume is a composite of two time slices at 2,490 ms and 2,536 ms in TWT to manifest
804 three BSRs. Horizon slices of H1, H3, and H5 are presented to show the basal shear surfaces of MTCs.
805 BD: background deposit.

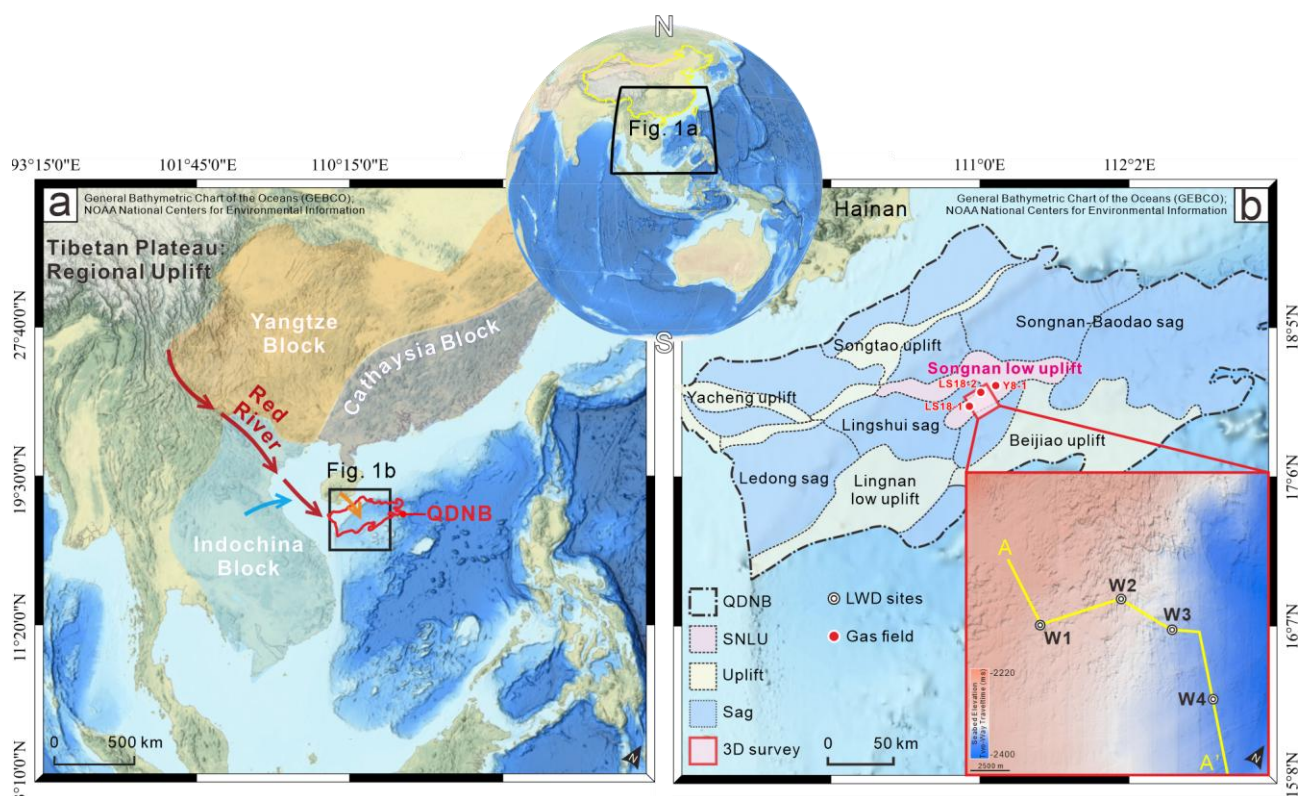
806 Figure A1. Demonstration of seismic-well tie using well W1 as an example.

Parameters	Notation	Unit	Value
Length of slope	L	m	4,800
Slope angle	α	$degree$	1.2
Density	ρ	$Kg \cdot m^{-3}$	1,700
Gravity acceleration	g	$m \cdot s^{-2}$	9.81
Yield stress	τ_0	Pa	8,000
Reference strain rate	$\dot{\epsilon}_r$	s^{-1}	0.1
Flow index	n	/	0.75
Numerical grid resolution	n_x	/	511
	n_y	/	127
CFL coefficient	CFL	/	0.2

807 Table 1

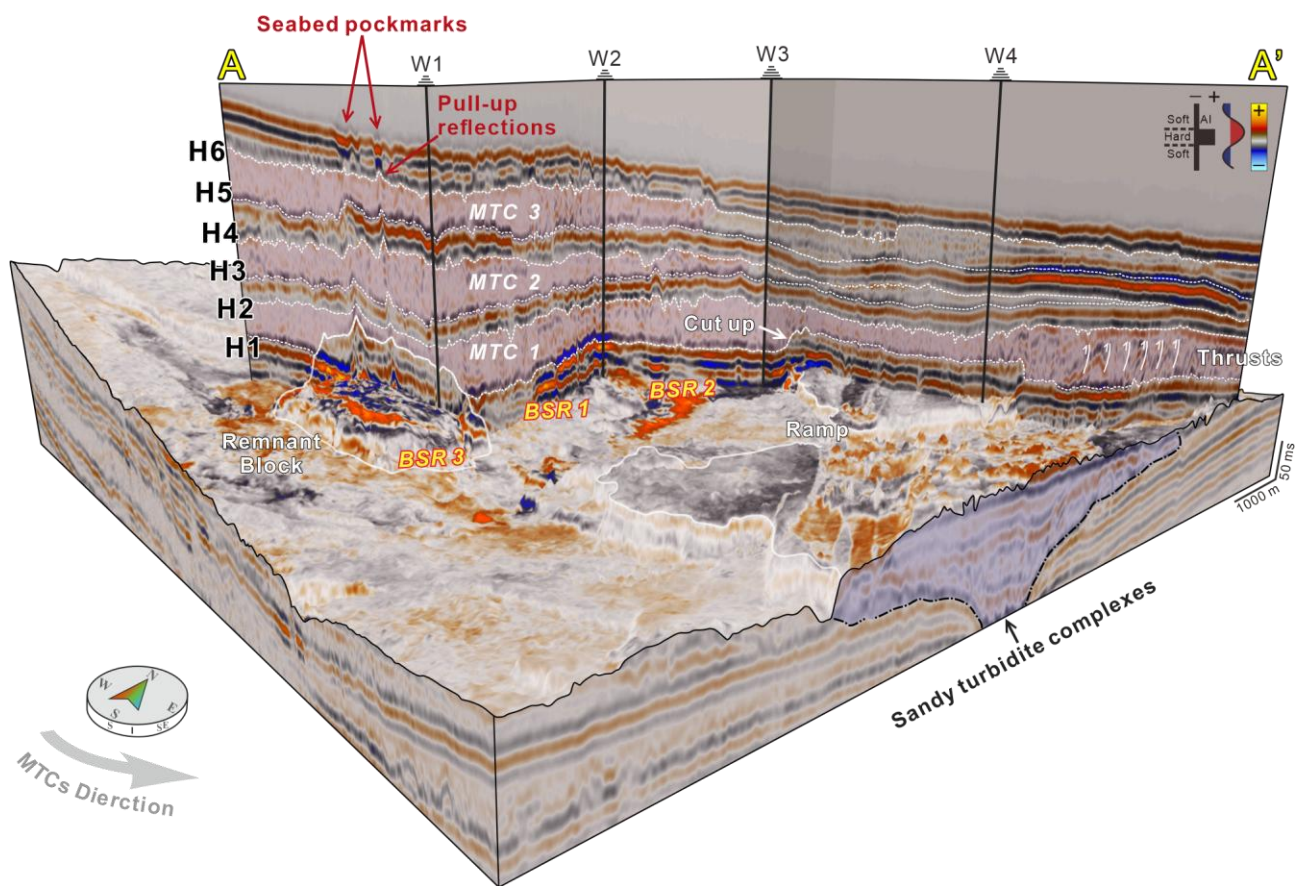
Amplitude anomaly	Petrophysical properties				Interpretation
	Density	Resistivity	P-velocity	Temperature	
BSR 1	Low $\sim 1.6 \text{ g/cm}^3$	Slightly high $\sim 2 \Omega m$	Low $\sim 1,600 \text{ m/s}$	High $\sim 8 \text{ }^\circ C$	Free gas sourced from the Songnan Low Uplift
BSR 2	Slightly high $\sim 1.85 \text{ g/cm}^3$	High $\sim 200 \Omega m$	High $\sim 2,300 \text{ m/s}$	Low $\sim 2 \text{ }^\circ C$	High-saturation gas hydrate ($\sim 90\%$ saturation)
BSR 3	Moderate $\sim 1.8 \text{ g/cm}^3$	Slightly high $\sim 2 \Omega m$	Slightly low $\sim 1,700 \text{ m/s}$	High $\sim 9 \text{ }^\circ C$	Coexistence of free gas and low- saturation gas hydrate ($\sim 10\%$ saturation)

808 Table 2



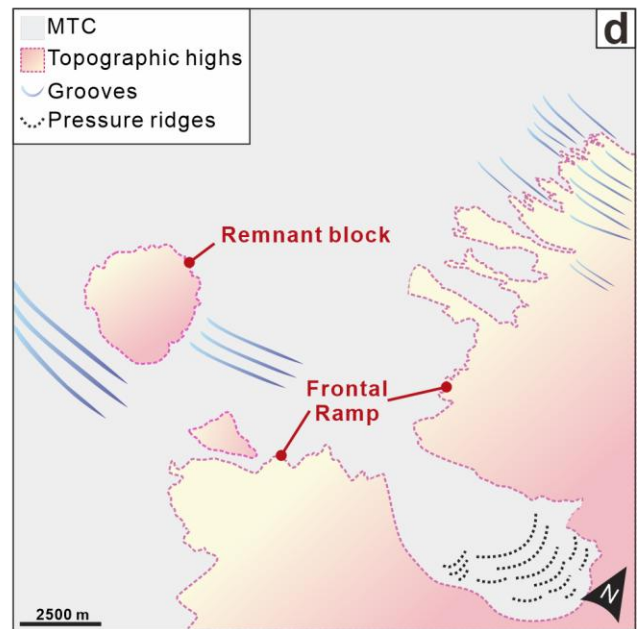
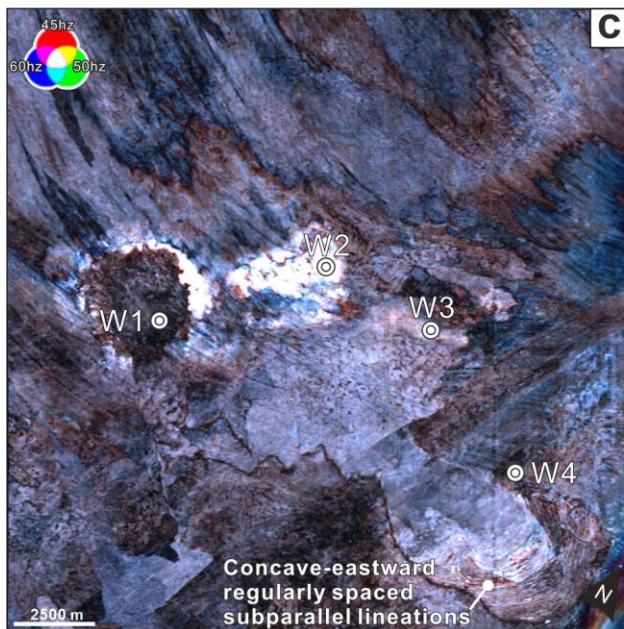
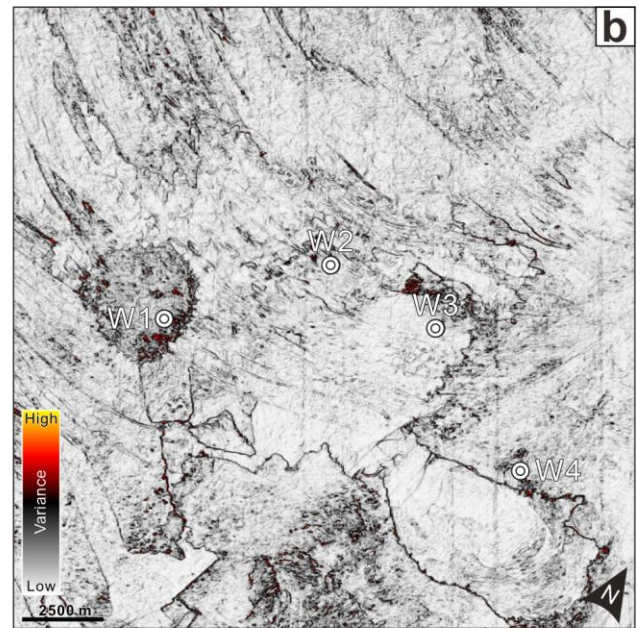
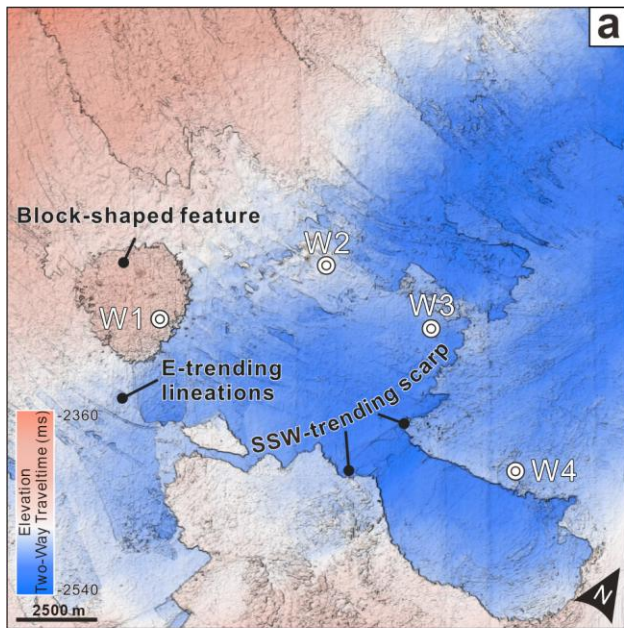
809

810 Figure 1



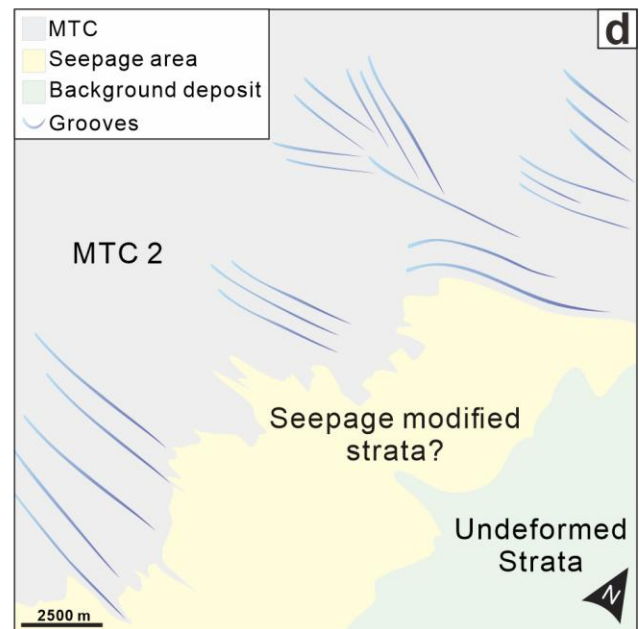
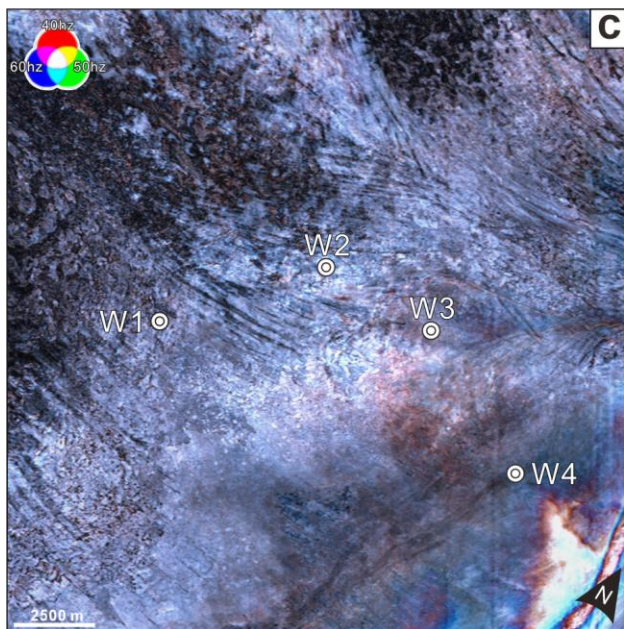
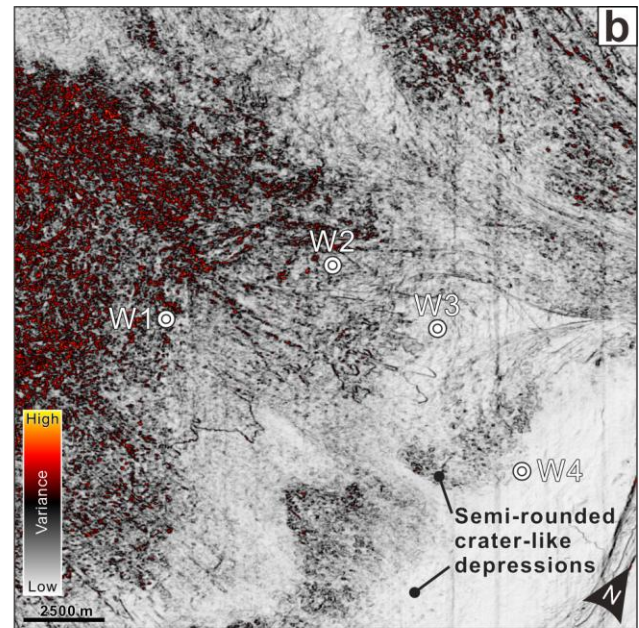
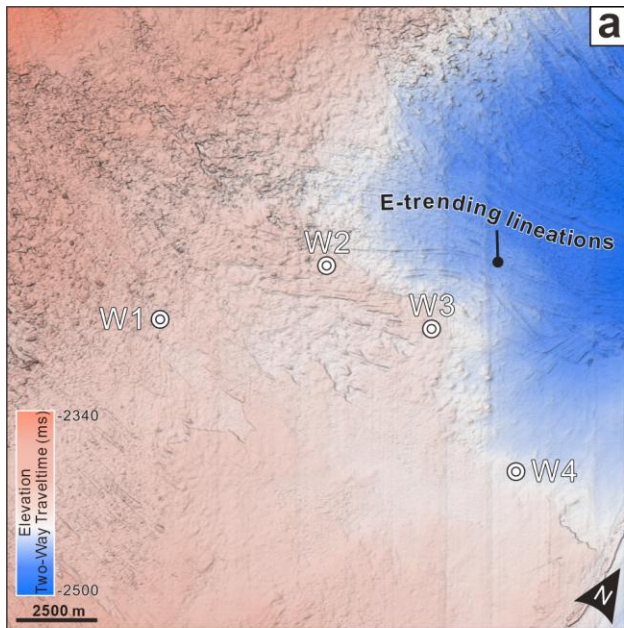
811

812 Figure 2



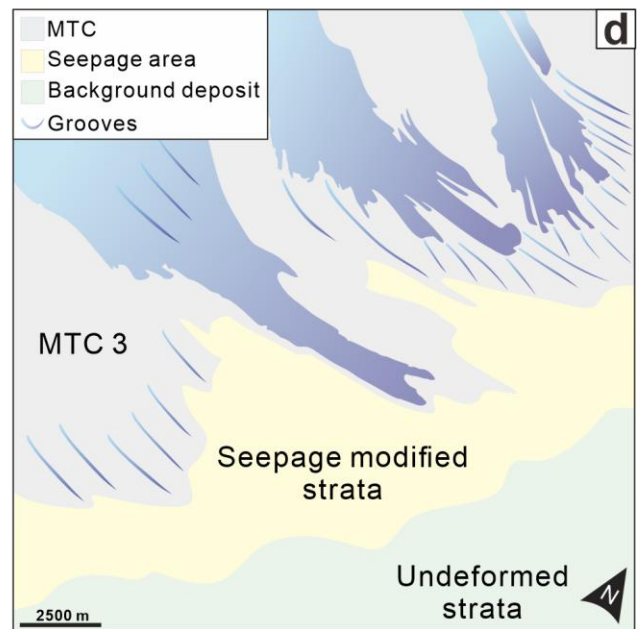
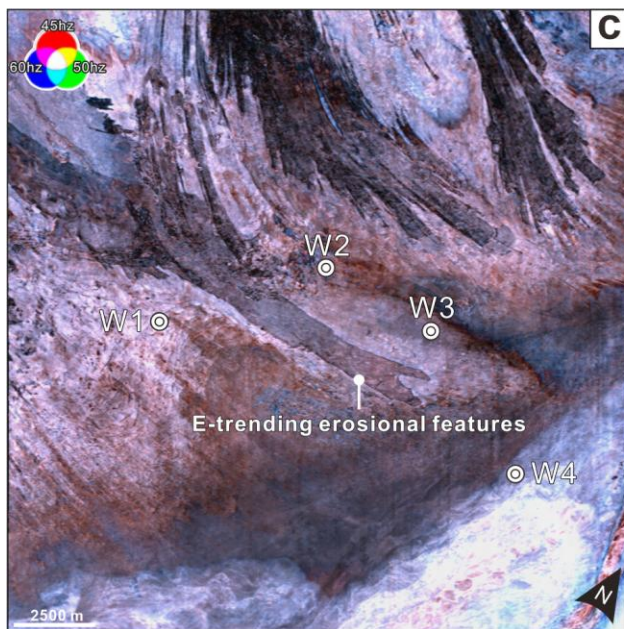
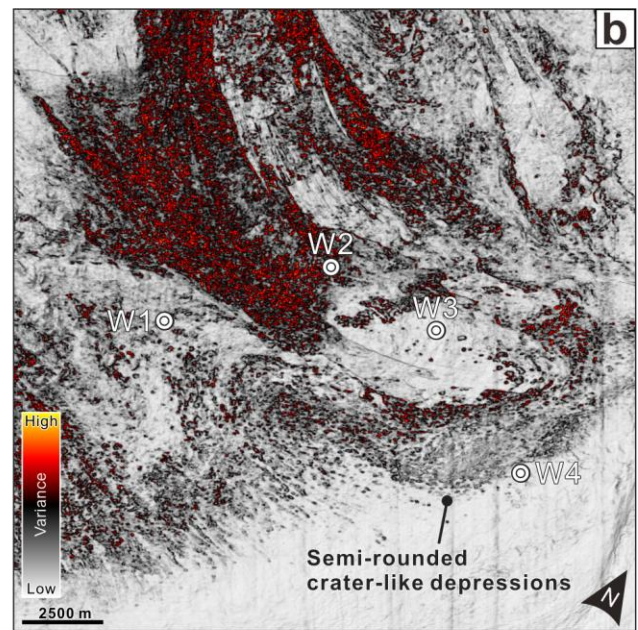
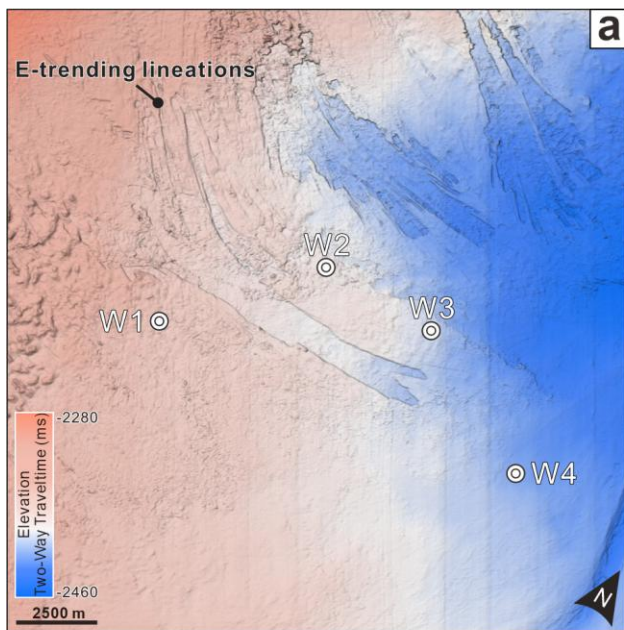
813

814 Figure 3



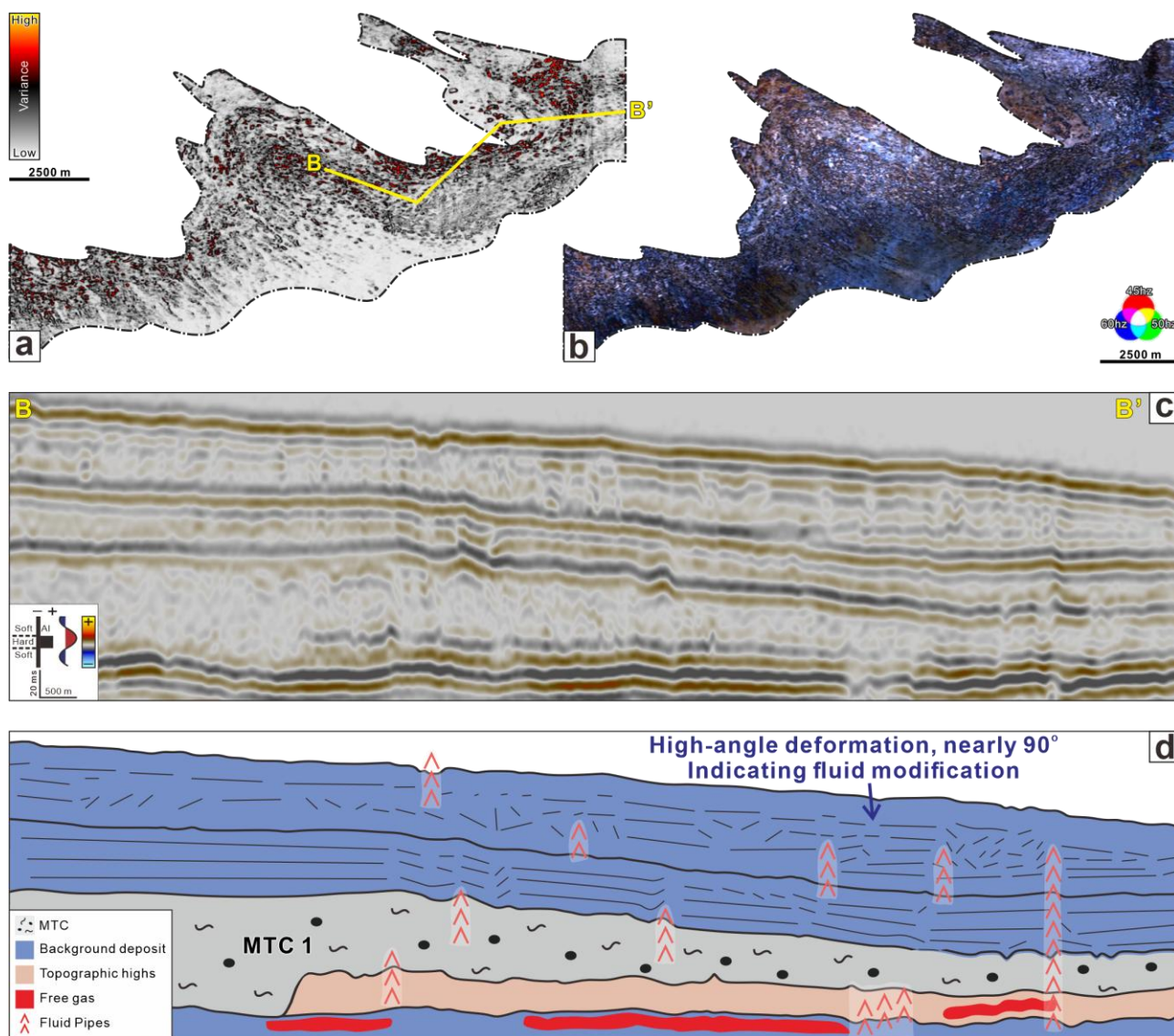
815

816 Figure 4



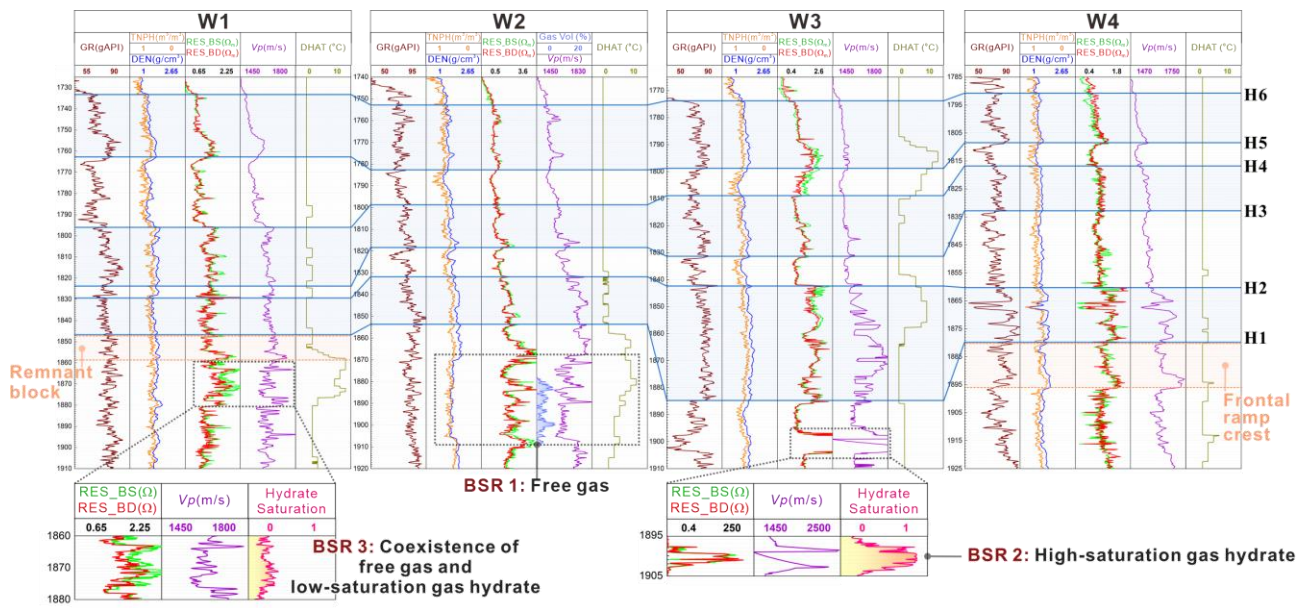
817

818 Figure 5



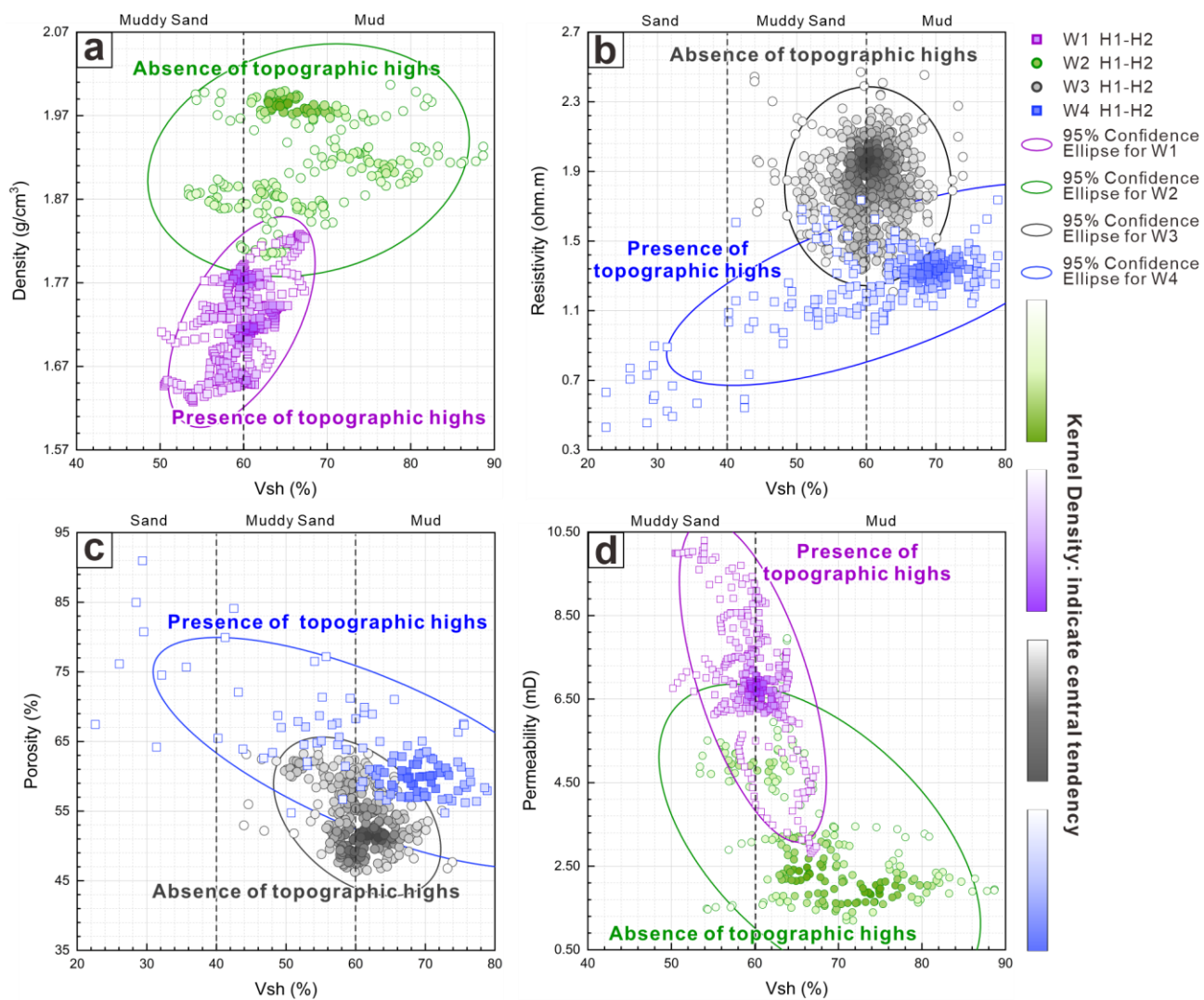
819

820 Figure 6



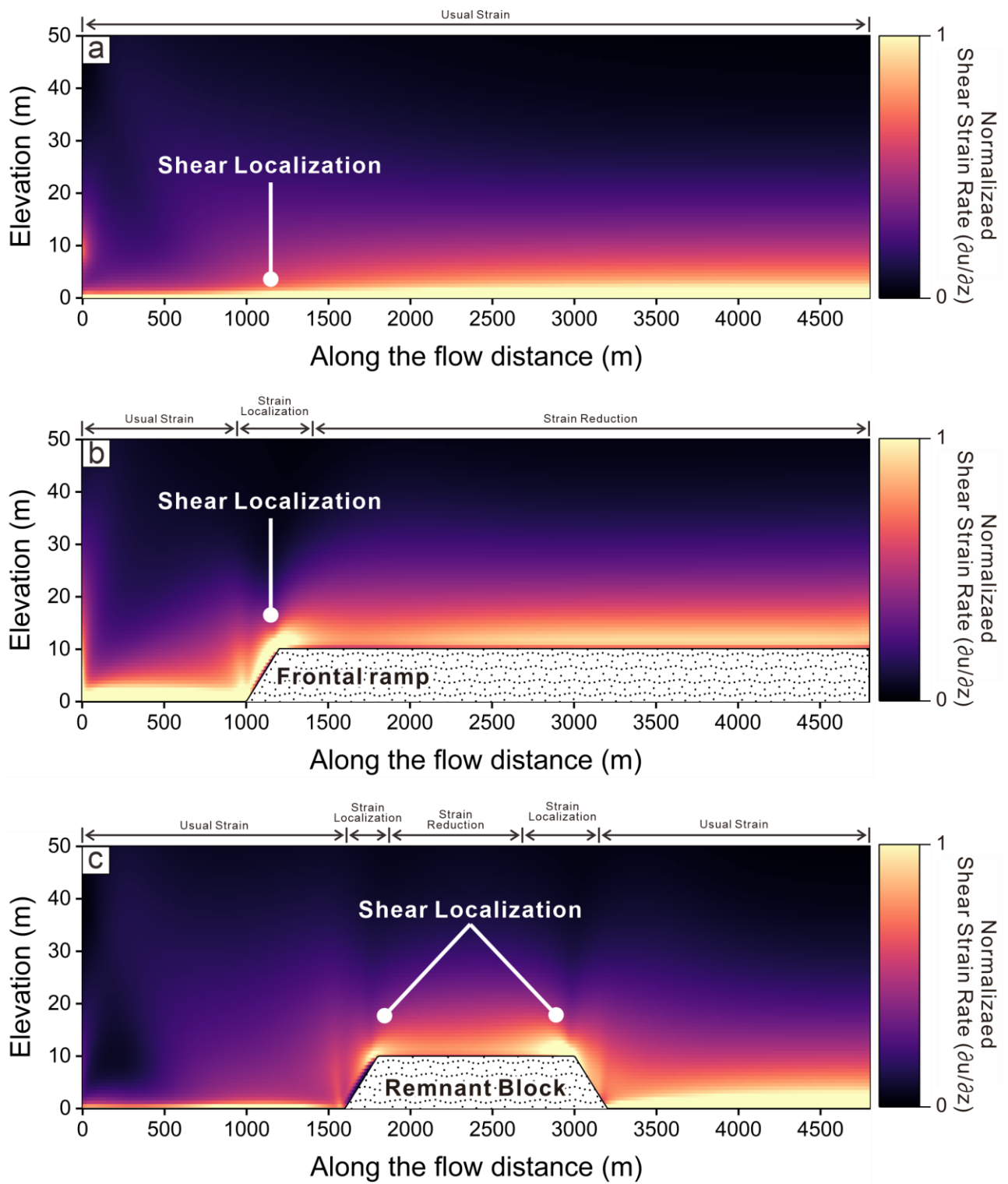
821

822 Figure 7



823

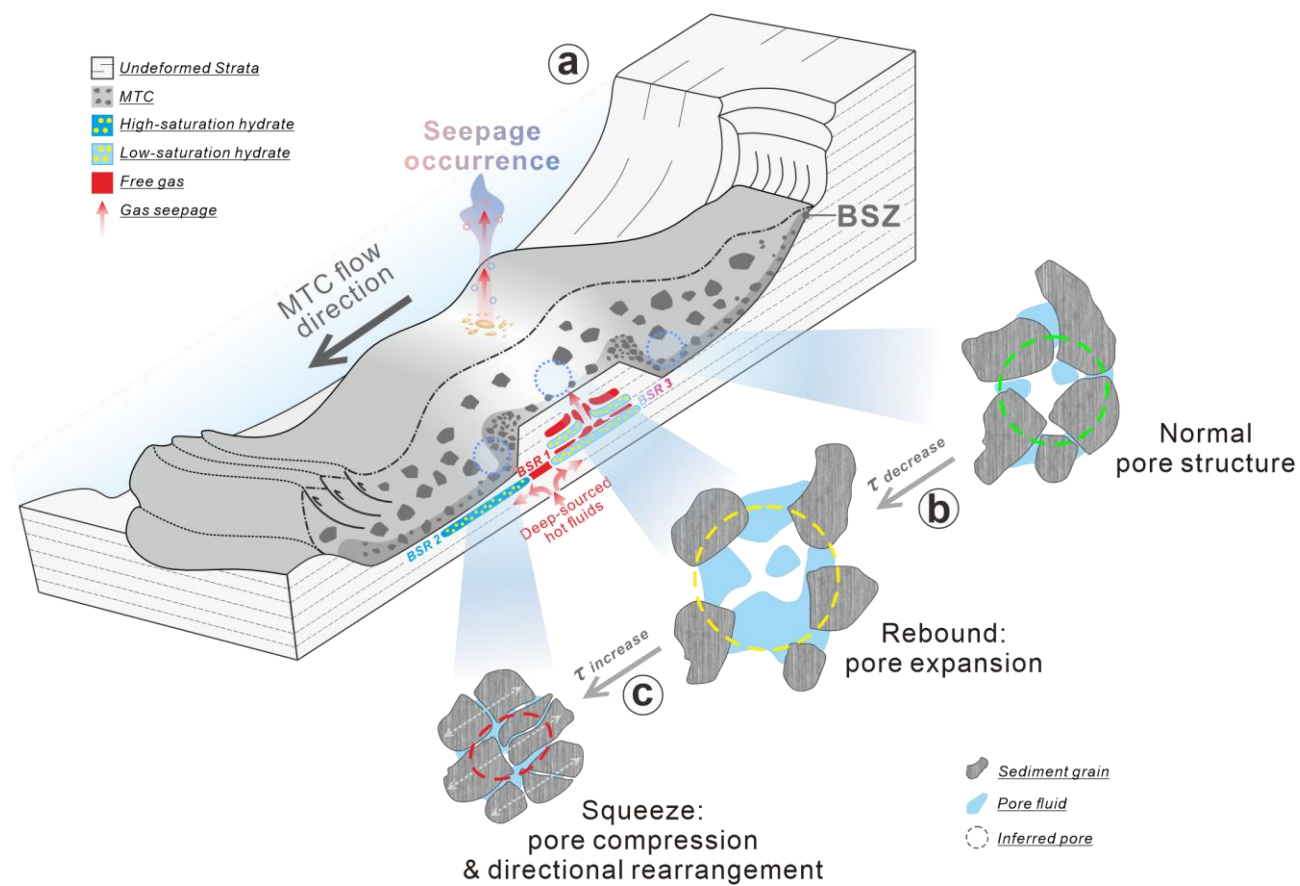
824 Figure 8



825

826 Figure 9

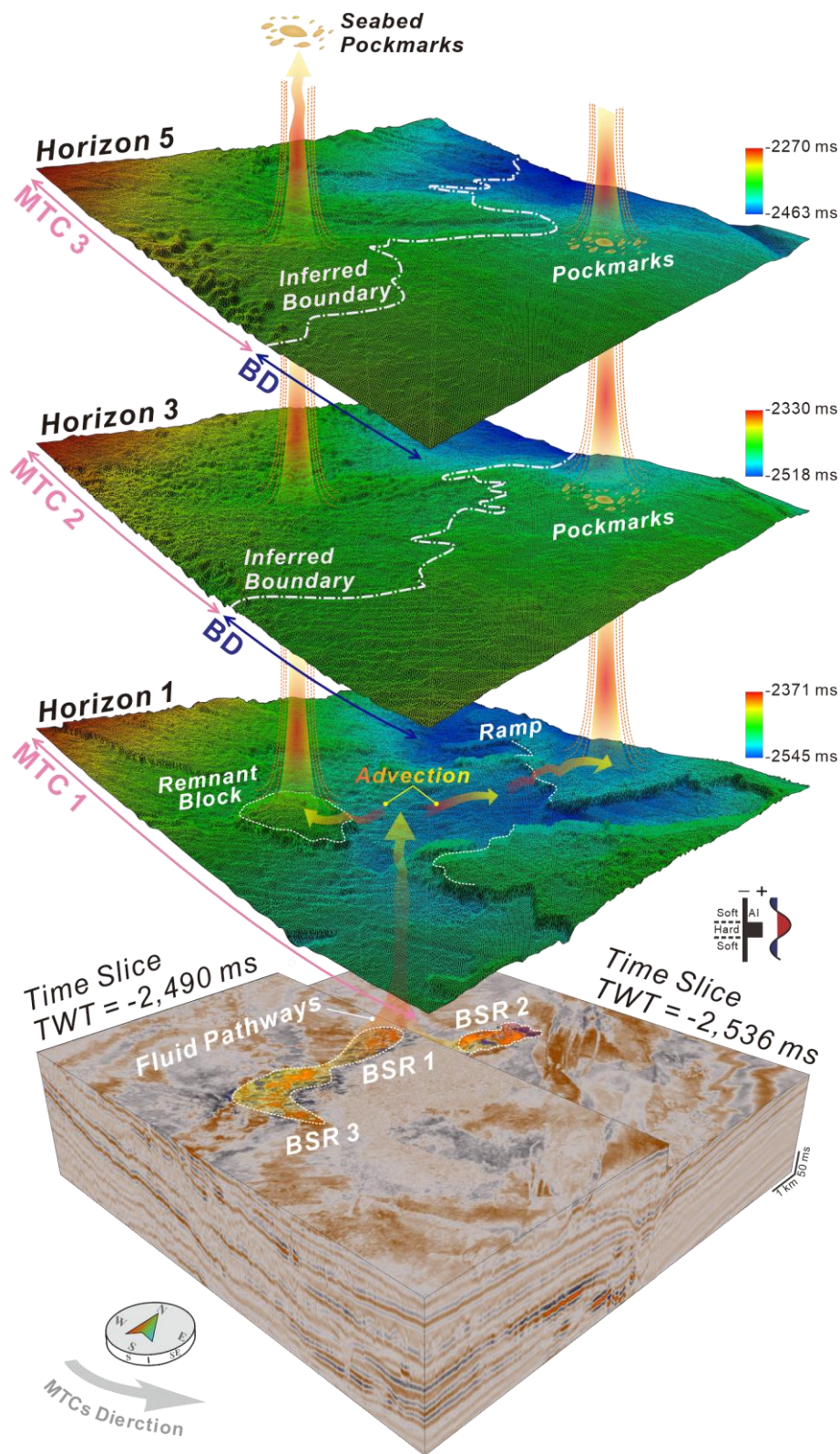
827



828

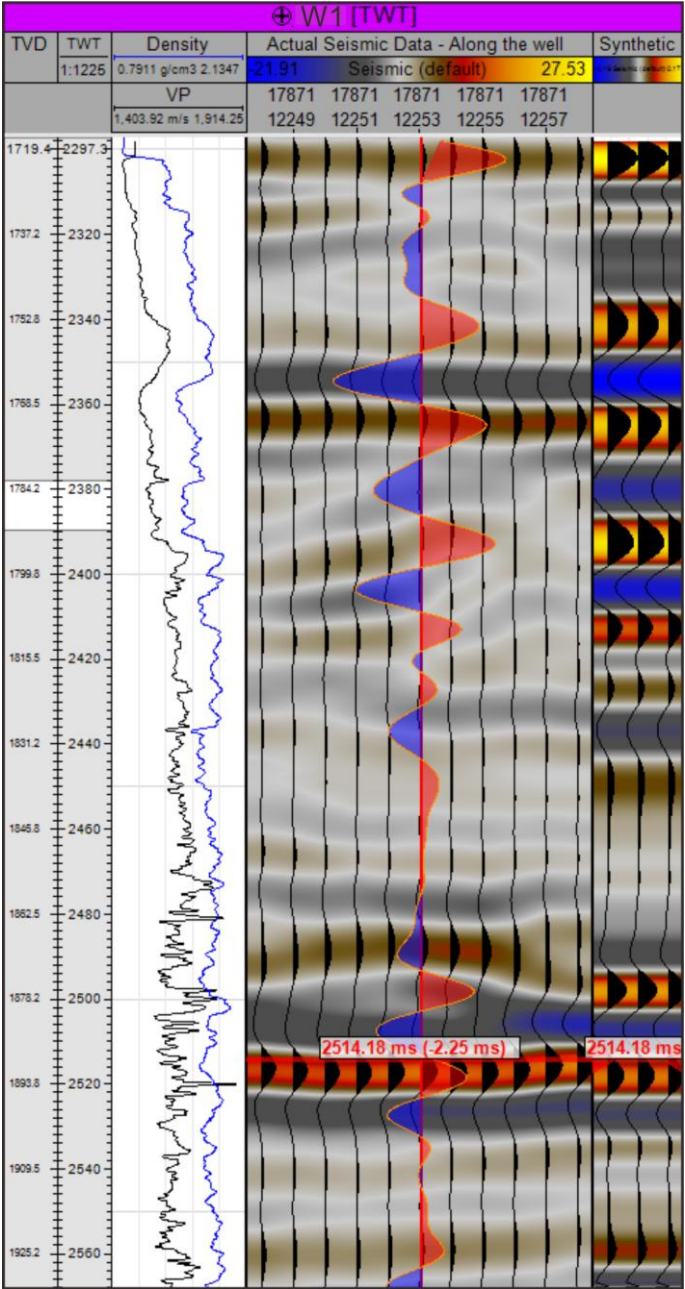
829 Figure 10

830



831

832 Figure 11



833

834 Figure A1